

The effect of a biosphere on the habitable timespan of stagnant-lid planets and implications for the atmospheric spectrum

Dennis Höning^{1*}, Ludmila Carone^{2*}, Philipp Baumeister³, Kathy L. Chubb^{2,4}, John Lee Grenfell³, Kaustubh Hakim^{5,6}, Nicolas Iro³, Benjamin Taysum³, and Nicola Tosi³

¹ Potsdam-Institute for Climate Impact Research, Potsdam, Germany
e-mail: dennis.hoening@gmail.com

² Space Research Institute, Austrian Academy of Sciences, Schmiedlstr. 6, A-8042 Graz, Austria

³ Institute of Planetary Research, German Aerospace Center (DLR), Berlin, Germany

⁴ Center for Exoplanet Science, University of St Andrews, North Haugh, St Andrews, UK

⁵ Royal Observatory of Belgium, Ringlaan 3, 1180 Brussels, Belgium

⁶ Institute of Astronomy, KU Leuven, Celestijnenlaan 200D, 3001 Leuven, Belgium

December 17, 2024

ABSTRACT

Temperature-dependent biological productivity controls silicate weathering and thereby extends the potential habitable timespan of Earth. Models and theoretical considerations indicate that the runaway greenhouse on Earth-like exoplanets is generally accompanied by a dramatic increase in atmospheric H₂O and CO₂, which might be observed with the upcoming generation of space telescopes. If an active biosphere extends the habitable timespan of exoplanets similarly to Earth, observing the atmospheric spectra of exoplanets near the inner edge of the habitable zone could then give insights into whether the planet is inhabited. Here, we explore this idea for Earth-like stagnant-lid planets. We find that while for a reduced mantle, a surface biosphere extends the habitable timespan of the planet by about 1 Gyr, for more oxidising conditions, the biologically enhanced rate of weathering becomes increasingly compensated for by an increased supply rate of CO₂ to the atmosphere. Observationally, the resulting difference in atmospheric CO₂ near the inner edge of the habitable zone is clearly distinguishable between biotic planets with active weathering and abiotic planets that have experienced a runaway greenhouse. For an efficient hydrological cycle, the increased bioproductivity also leads to a CH₄ biosignature observable with JWST. As the planet becomes uninhabitable, the H₂O infrared absorption bands dominate, but the 4.3-micron CO₂ band remains a clear window into the CO₂ abundances. In summary, while the effect of life on the carbonate-silicate cycle leaves a record in the atmospheric spectrum of Earth-like stagnant-lid planets, future work is needed especially to determine the tectonic state and composition of exoplanets and to push forward the development of the next generation of space telescopes.

1. Introduction

The search for life on planets beyond our Solar System is receiving a boost with the new and upcoming generation of space telescopes enabling the characterisation of planetary atmospheres (e.g. Gialluca et al. 2021; Faucher et al. 2019; Lin & Kaltenegger 2022). A detection of a chemical disequilibrium – such as oxygen together with methane – would indicate that oxygen is replenished continuously, and oxygenic photosynthesis is the most efficient way to maintain this disequilibrium (e.g. Schwieterman et al. 2018; Krissansen-Totton et al. 2022).

A detailed characterisation of planetary atmospheres, however, requires expensive, long-term space telescope observations. Given the vast number of exoplanets and the limitations in observational time and cost, it is essential to prioritise the study and observations of planets that are most likely candidates to support the emergence and maintenance of life.

To first order, planetary habitability can be assessed using the concept of the habitable zone, which is the distance of a planet to the star that would allow for liquid water on the planetary surface. Besides the stellar luminosity and the orbital distance of the planet, greenhouse gases in the planetary atmosphere, in particular CO₂, determine the planetary surface temperature and thereby its potential habitability (e.g. Kopparapu et al. 2013; Ramirez 2018).

The concentration of atmospheric CO₂ is controlled by numerous complex processes involving the interior, the surface, and the atmosphere (e.g. Foley 2015; Kruijver et al. 2021; Oosterloo et al. 2021). Depending on the composition and thermal state of the mantle, CO₂ is released into the atmosphere via volcanism. If liquid surface water and an active hydrological cycle are present on the planet, CO₂ reacts with rainwater to form carbonic acid, which can dissolve silicate rocks. Weathering products are washed into the ocean, where calcium carbonate is precipitated. If the planet possesses Earth-like plate tectonics, carbonates are recycled back into the deep interior at subduction zones (e.g. Sleep & Zahnle 2001; Kasting & Catling 2003; Catling & Kasting 2017).

On a planet without plate tectonics (i.e. on a stagnant-lid planet), carbonates are not subducted but instead accumulate on the seafloor where they are eventually buried by new lava flows, as long as the planet can sustain active volcanism. Therefore, layers of carbonated rocks gradually migrate downwards, heating up until they become unstable. Through this decarbonation reaction, CO₂ is released back into the atmosphere, thereby closing the carbonate-silicate cycle on a timescale shorter than for planets with active plate tectonics (Foley & Smye 2018; Höning et al. 2019; Baumeister et al. 2023).

In our Solar System, Earth is the only planet with plate tectonics. Theory and simulations indeed indicate that a stagnant lid is a more likely outcome of mantle convection (e.g. Ogawa et al.

* DH and LC contributed equally to this paper.

1991; Davaille & Jaupart 1993; Moresi & Solomatov 1995). In fact, in the absence of efficient weakening mechanisms, the strong temperature dependence of the viscosity of mantle rocks naturally leads to the formation of a highly viscous, immobile, and conductive lid, extending from the surface down to the base of the thermal lithosphere (Schubert et al. 2001). In this paper, we specifically explore the habitability of stagnant-lid planets.

Outgassed volatiles originate from surface lavas that are the product of partial melting of the upper mantle. The mantle composition thus plays an important role in the buildup and long-term evolution of the atmosphere and in turn on habitability. In particular, the mantle redox state controls whether reduced species (such as H_2 , CO , or CH_4) or oxidised species with a strong greenhouse potential (such as H_2O and CO_2) are ultimately released into the atmosphere (see Gaillard et al. 2021, for a recent review).

Deriving the interior composition and redox state of exoplanets is difficult and fraught with large uncertainties. In principle, rock-building elemental abundances of the host star could be used as proxies for the interior composition (e.g. Dorn et al. 2015; Brugger et al. 2017; Unterborn & Panero 2019), but the link between the two is not straightforward (Plotnykov & Valencia 2020; Schulze et al. 2021). The spectroscopic study of ‘polluted’ white dwarfs, which contain traces of accreting rocky bodies previously orbiting around them, suggests that the oxidation state of these bodies is similar to that of moderately reduced bodies of the Solar System such as Mars, although the discussion remains open about this (Doyle et al. 2019). For this work, we treated the redox state of the mantle as a free parameter and followed the approach of redox melting that Grott et al. (2011) applied to Mars and Tosi et al. (2017) and Godolt et al. (2019) did to exoplanets, focusing mainly on volcanic outgassing of CO_2 .

Besides tectonics and interior composition, a key factor that controls the climate and the habitability – at least on Earth – is its biosphere. Land vegetation enhances continental weathering, for example as roots of trees break rocks and thereby amplify the weatherable surface area, or with lichens that provide a continuously humid environment (e.g. Berner 1992; Schwartzman & Volk 1989, 1991). In addition, microbes and fungi produce acids that enhance silicate weathering. Since the biological productivity, and in turn the biological enhancement of weathering, increase with temperature and CO_2 , negative feedback to temperature oscillations emerges: increasing temperature amplifies the biological enhancement of weathering by which CO_2 is effectively removed from the atmosphere, causing a decrease in the global mean surface temperature. This feedback process is particularly important as it can dampen the increase in surface temperature as stellar luminosity rises with time and can therefore potentially extend the habitable timespan of the planet (Lenton & von Bloh 2001). Marine organisms also provide negative feedback to climate oscillations. However, this effect is mainly important on sub-million-year timescales (Höning 2020). Because our models are applicable on longer timescales (>100 Myr), the effect of marine organisms is neglected in the present study.

For stagnant-lid planets, the effect of a surface biosphere on the surface habitability is not trivial. Even though biological enhancement of weathering provides negative feedback to rising temperatures by enhancing the drawdown of CO_2 , carbonates are precipitated at a higher rate with an active biosphere, which enhances the carbon concentration of the crust. As the CO_2 is subsequently released into the atmosphere when carbonates become unstable, biological enhancement of weathering indirectly raises the rate at which CO_2 is released into the atmosphere. In this paper, we explore these opposing effects.

A key consequence of weathering is that most of the near-surface CO_2 is trapped in the form of carbonates, leaving only a small fraction of CO_2 in the atmosphere for planets inside the habitable zone. By the time the moist or runaway greenhouse limits are reached, oceans evaporate and weathering becomes increasingly inefficient or eventually ceases (Kasting 1988). Since CO_2 will continue to be released into the atmosphere through mantle degassing, atmospheric CO_2 will rapidly increase. Such a bimodal distribution of CO_2 for planets on both sides of the habitable zone might be statistically identified by measuring CO_2 levels (Bean et al. 2017; Graham & Pierrehumbert 2020; Schlecker et al. 2024). Measurements of CO_2 levels and Sun-like insolation with future mission concepts for at least 83 planets in the habitable zone have been suggested to determine if weathering is a universal phenomenon (Lehmer et al. 2020).

For stagnant-lid planets, the rise of atmospheric CO_2 after runaway greenhouse is particularly strong, since mantle degassing is accompanied by self-accelerating crustal decarbonation: with increasing surface temperature, the depth at which decarbonation occurs gradually moves upwards, releasing even more CO_2 into the atmosphere. Höning et al. (2021) find that the atmospheric CO_2 partial pressure increases by ≈ 2 orders of magnitude within ≈ 100 Myr. We note that only a significant surface temperature rise – such as during runaway greenhouse – noticeably affects the decarbonation depth; in contrast, as long as the planet’s surface temperature remains within the habitable range, the decarbonation depth is almost solely controlled by the mantle temperature (Höning et al. 2021).

If an active surface biosphere enhances the habitable timespan of exoplanets, it would shift the moment in time – or the critical stellar distance – at which the atmospheric CO_2 dramatically increases. Planets of a similar composition, age, and incident insolation could then either have small atmospheric CO_2 content – if they are inhabited, with an active biosphere that enhances continental weathering – or have a high atmospheric CO_2 content if the planet is abiotic and underwent a runaway greenhouse in its past. Determining the atmospheric CO_2 concentration of exoplanets near the inner edge of the habitable zone could then not only reveal whether or not the planet is habitable, but could also yield insights into a potentially active surface biosphere.

The goals of this paper are threefold. First, we aim to assess whether, and to which extent, a biosphere extends the habitable timespan of stagnant-lid planets. Second, we explore the differences in atmospheric CO_2 and CH_4 levels between inhabited (biotic) planets and uninhabited (abiotic) planets that have experienced a runaway greenhouse due to a shorter habitable timespan. Finally, we evaluate the observational potential for detecting these differences by modelling transmission measurements from the James Webb Space Telescope (JWST).

2. Model

We employed a coupled interior-atmosphere evolution model for stagnant-lid planets (Grott et al. 2011; Tosi et al. 2017; Godolt et al. 2019; Höning et al. 2021; Baumeister et al. 2023). The interior thermal evolution is based on a standard parameterisation of convective heat transport based on solving the energy-conservation equations of the core, mantle, and stagnant lid. The convective heat flux is derived from boundary layer theory (Schubert et al. 2001) and the viscosity is strongly temperature-dependent (Grasset & Parmentier 1998; Choblet & Sotin 2000).

Whenever the upper mantle temperature exceeds the solidus of dry peridotite (Katz et al. 2003), the accompanying volume

Table 1. Constants used in the model.

Parameter	Description	Value
α	Constant, Eq. 1	0.33 ⁽¹⁾
E_a	Eff. activation energy for silicate weathering	$3.8 \cdot 10^4$ J mol ⁻¹ ⁽²⁾
M_O	Ocean mass	$1.35 \cdot 10^{21}$ kg ⁽¹⁾
a_{min}	Min. atm. CO ₂ for plant growth	10 ppm ⁽³⁾
$B_{T,E}$	Constant	0.8352 ppm ⁽⁴⁾
$a_{1/2}$	Constant	181 ppm ⁽⁴⁾
$F_{sf,E}$	Pre-industrial seafloor-weathering rate	$1.75 \cdot 10^{12}$ mol yr ⁻¹ ⁽⁵⁾
$T_{s,E}$	Pre-ind. surf. temperature	287 K
$p_{CO_2,E}$	Pre-ind. atm. CO ₂	280 ppm
ξ	Pre-ind. fraction of abiotic weathering	0.25 ⁽⁶⁾
f_{degas}	Frac. temp. crustal carbon reservoir that degasses	0.02 ⁽⁷⁾

Sources: ⁽¹⁾ Krissansen-Totton & Catling (2017), ⁽²⁾ Palandri & Kharaka (2004), ⁽³⁾ Bergman et al. (2004), ⁽⁴⁾ Höning (2020), ⁽⁵⁾ Mills et al. (2014), ⁽⁶⁾ upper value considered by Lenton et al. (2018), ⁽⁷⁾ Höning et al. (2019).

of melt is calculated assuming a linear increase in melt fraction between solidus and liquidus and accounting for latent heat. The melt is enriched in heat-producing elements and the residual mantle is depleted in those according to a partition coefficient. The produced melt is the only source of new basaltic crust and therefore essential for weathering. The melt is also enriched in CO₂ according to the parameterisation introduced by Grott et al. (2011), which assumes that carbon can be supplied to the melt as long as the mantle is sufficiently hot to undergo partial melting and in a concentration that only depends on the mantle oxygen fugacity. The generated melt volume is extracted instantaneously to the surface where CO₂ in excess of its solubility in basaltic melts is released into the atmosphere. The CO₂ outgassing rate therefore increases with the mantle oxygen fugacity.

We based the calculation of silicate weathering on stagnant-lid planets F_w on Höning et al. (2019) but extended it to account for both the temperature- and CO₂ dependence of weathering:

$$F_w^* = \omega^* B^* (p_{CO_2}^*)^\alpha \exp\left(\frac{E_a}{R} \left(\frac{1}{T_{s,E}} - \frac{1}{T_s}\right)\right), \quad (1)$$

where ω^* is the relative weatherability (see below), B is the biological enhancement of weathering, p_{CO_2} is the partial pressure of CO₂ in the atmosphere, T_s is the surface temperature, α is a constant, E_a is the activation energy and R is the gas constant. Here and in the following, the index E denotes present-day Earth variables and the asterisk denotes variables scaled with their present-day Earth value, that is, $F_w^* = F_w/F_{w,E}$. Constants and free parameters are given in tables 1 and 2, respectively.

As in Höning et al. (2019), we scaled the relative weatherability ω^* on stagnant-lid planets to seafloor weathering on present-day Earth, since both rates directly depend on crustal production:

$$\omega^* = \frac{X_E \xi_E}{f_E} \left(\frac{dM_{cr}}{dt}\right), \quad (2)$$

where $\frac{dM_{cr}}{dt}$ is the crustal production rate and X_E , ξ_E , and f_E are the present-day Earth values of mid-ocean ridge CO₂ concen-

Table 2. Free parameters used in the model.

Parameter	Description	Value
d	Stellar distance	0.7 AU – 1.0 AU
f_{O_2}	Mantle oxygen fugacity	IW-0.2 (IW-0.4, IW+0)
$T_{m,E}$	Ini. mantle temp.	1900 K (1850 K, 1950 K)
η_{ref}	Ref. mantle visc.	10^{21} Pa s (10^{20} Pa s, 10^{22} Pa s)

tration in the melt, fraction of seafloor weathering, and fraction of buried carbonates that enter the mantle. We note that the scaling to seafloor weathering solely serves the purpose of obtaining a relationship between the weatherability and rate at which fresh basaltic crust is produced; mid-ocean ridges producing fresh seafloor do not exist on stagnant-lid planets.

Modelling the biological enhancement of weathering (factor B in Eq. 1), we restricted ourselves to land plants as present on the modern Earth. Therefore, the model is strictly valid only for planets with a biosphere similar to that having emerged on Earth only 400-500 million years ago. We further assumed that a constant fraction ξ of continental weathering is not affected by bioactivity whereas the rest ($1-\xi$) depends on plant productivity (Höning 2020; Lenton & von Bloh 2001; Caldeira & Kasting 1992). Following Höning (2020), we modelled plant productivity as a function of the surface temperature and atmospheric CO₂

$$B^* = \xi + (1 - \xi) \cdot B_T^* \cdot B_{CO_2}^*, \quad (3)$$

where B_T^* and $B_{CO_2}^*$ are the temperature- and CO₂-dependent terms of plant productivity. The temperature dependence follows a parabolic function of temperature

$$B_T^* = B_{T,E}^{-1} \left(1 - \left(\frac{T_s(^{\circ}\text{C}) - 25^{\circ}\text{C}}{25^{\circ}\text{C}}\right)^2\right), \quad (4)$$

and the CO₂-dependence follows a Michaelis-Menton function

$$B_{CO_2}^* = \frac{(p_{CO_2} - a_{min})(p_{CO_2,E} - a_{min} + a_{1/2})}{(p_{CO_2} - a_{min} + a_{1/2})(p_{CO_2,E} - a_{min})}, \quad (5)$$

where $B_{T,E}$, a_{min} and $a_{1/2}$ are constants (see Höning 2020, for details). Specifically, we modelled bioproductivity to increase with temperature up to 25°C and then to decrease at higher temperatures, so that the negative feedback is only effective until that specific surface temperature.

Carbonates were assumed to accumulate on the seafloor and be buried by new lava flows. Buried carbonated crust was tracked downwards until decarbonation occurs (Höning et al. 2019; Baumeister et al. 2023). Decarbonation was assumed to occur through the breakdown of dolomite (Foley & Smye 2018). For more details, the reader is referred to Höning et al. (2019, 2021).

Water vapour and CO₂ were considered as the only greenhouse gases and a radiative grey atmosphere model was used to calculate greenhouse heating (Catling & Kasting 2017). Water outgassing from the mantle was neglected and the surface water budget was assumed to resemble Earth's. In synthesis, the surface temperature T_s was calculated as a function of the equilibrium temperature T_{eq} and of the optical depth of the atmosphere in the infrared τ :

$$T_s^4 = T_{eq}^4 \left(1 + \frac{3\tau}{4}\right), \quad (6)$$

where

$$T_{eq}^4 = \frac{(1 - A)S_{sun}}{4\sigma}, \quad (7)$$

where S_{sun} is the insolation at the top of the atmosphere, σ is the Stefan-Boltzmann constant, and A is the albedo. The optical depth τ simply considers the additive contribution of the optical depths of H_2O and CO_2 expressed in terms of the corresponding absorption coefficients (see Höning et al. 2021; Baumeister et al. 2023, for details).

Höning et al. (2021) compares the global mean temperature throughout the habitable period obtained by this model with the outcome of the 3-D global circulation model ROCKE-3D (Way et al. 2017; Way & Del Genio 2020) and obtain good agreement. We assumed that the modelled exoplanet has Earth-like size and mass, an albedo of 0.35, and orbits a Sun-like star accounting for stellar evolution. For application to a TRAPPIST-1-like star, we assumed that TRAPPIST-1e is the planet that is best suited for the scenarios explored in this work as it also orbits at the inner edge of its host star’s habitable zone.

Using our baseline model, we further explored exemplary snapshots in time of our sample planets with an atmosphere model. For the habitable, biotic cases (with will be later referred to as scenarios 1 and 2, see Table 3), we used the fully self-consistent atmosphere-chemistry model 1D TERRA (Wunderlich et al. 2020), which takes the surface pressures of CO_2 and H_2O from the geophysical model as well as 0.2 bar O_2 and 1 bar N_2 as input parameters. The model 1D TERRA also assumes an active hydrological cycle, where we differentiated between a ‘dry’ or ‘moist’ composition. The effect of bioproductivity on the source fluxes in 1D TERRA, as described in (Wunderlich et al. 2020, Table 4), was established by taking into account the CO_2 - and temperature-dependence of bioproductivity (Eq. 4 and 5), resulting in biogenic fluxes of constituents such as CH_4 relative to present-day Earth by a factor of 1.905 and 1.805 for scenarios 1 and 2, respectively. For more details on the model, the reader is referred to section 3.2 and Appendix D.

For the abiotic cases (scenarios 3 and 4), we enter an atmosphere regime with uncertainties in atmospheric escape for a runaway-greenhouse scenario, in particular around M dwarfs (Boukrouche et al. 2021; Owen 2019; Tian 2015; Gronoff et al. 2020) and in the role of photochemistry in dense CO_2 -dominated atmospheres like Venus (Stolzenbach et al. 2023; Wilson et al. 2024; Petkowski et al. 2024). For these scenarios, we used a simpler model than for the biotic scenarios (Appendix A). We assumed that water vapour cannot condense out of the atmosphere and further assumed strong vertical mixing. In these steam-dominated atmospheres, the atmospheric content of both CO_2 and H_2O was determined by the geophysical model and assumed to be constant to first order, which is a typical assumption for runaway-greenhouse atmospheres (e.g. Boukrouche et al. 2021; Lichtenberg et al. 2021). We again assumed 1 bar N_2 to which the respective partial pressures of H_2O and CO_2 are added. We then applied the multispecies pseudoadiabat prescription by Graham et al. (2021) to construct pressure–temperature profiles. For the ‘steam atmospheres’, water condensation is in equilibrium with evaporation and rainout was neglected such that the strong latent heat effect of water dominates the temperature of the upper atmosphere.

Further, we explored a ‘desiccated’ scenario, where we assumed to first order that the steam scenario 4 results in complete desiccation, which we mimicked by removing by H_2O completely while the resulting CO_2 surface pressures is about

10% of that of current Venus (Table 3). Readers can refer to Appendix A for a more detailed overview. We further note that the complete removal of about one terrestrial ocean equivalent of water (270 bar atmospheric pressures) in a steam-dominated atmosphere can be assumed to be a fairly efficient process occurring within a time interval shorter than 100 million years (e.g. Abe et al. 2011; Barth et al. 2021).

3. Results

The results section is structured as follows. In section 3.1, we explore the effect of a biosphere on the partial pressure of atmospheric CO_2 focusing on the transition from a habitable to an uninhabitable climate. We start with our baseline model for which we used a mantle oxidation state of IW-0.2 (that is, a mantle oxidation state of 0.2 log units below the iron-wüstite-buffer), an initial mantle temperature of 1900 K, and a reference mantle viscosity of 10^{21} Pa s. We chose this parameter combination for our baseline model for illustrative purposes as it results in a habitable period between 1.5 and 5 Gyr depending on the stellar distance, which we vary between 0.7 and 1 AU. Following this, we explore the sensitivity of our results to these parameters. In section 3.2, we then use our baseline model as an example to study the observational signatures associated with the transition towards uninhabitable conditions.

3.1. Impact of bioproductivity on atmospheric CO_2

The bimodal distribution of atmospheric CO_2 (Fig. 1) indicates a transition from habitable surface conditions to uninhabitable conditions after the runaway greenhouse. The closer the planet is to the star, the earlier the runaway greenhouse sets in. For our baseline model, the habitable period of a lifeless (abiotic) planet (Fig. 1a) is shorter than for an inhabited (biotic) planet (Fig. 1b). The reason is the biologically enhanced rate of weathering, removing CO_2 at a rate much higher than for the lifeless planet. Fig. 1c depicts the difference between the two planets, indicating an extension of the habitable period by up to 1 Gyr if life is present (dark blue region in Fig. 1c).

In addition to the stellar distance, planet age, and a potential biosphere, other planet-specific parameters can control the atmospheric CO_2 and therefore the habitable timespan of stagnant-lid planets. In particular, the three parameters – mantle oxidation state, initial mantle temperature, and reference mantle viscosity – have a strong impact on the CO_2 outgassing rate throughout the evolution of stagnant-lid planets and therefore shift the moment in time the planet becomes uninhabitable. In Fig. 2, we systematically show the impact of the mantle oxygen fugacity (a–f), initial mantle temperature (g–l), and reference mantle viscosity (m–r).

For more reducing conditions (f_{O_2} =IW-0.4, Fig. 2, panels a–c), the runaway greenhouse sets in later than for our baseline model (f_{O_2} =IW-0.2, Fig. 1). This is due to the fact that the rate of CO_2 outgassing roughly changes proportionally to variations of the oxygen fugacity with respect to the IW-buffer (Grott et al. 2011; Tosi et al. 2017). We also find that the impact of a biosphere is larger in this case, extending the habitable timespan by up to 2 Gyr. On the contrary, for more oxidising conditions (f_{O_2} =IW+0, Fig. 2, panels d–f), the effect of biologically enhanced weathering can be overcompensated by the enhanced crustal carbon concentration, which is an indirect effect of the enhanced weathering rate, leading to an enhanced rate of crustal decarbonation. As a result, the habitable period could become shorter altogether. We note that this result is exclusively

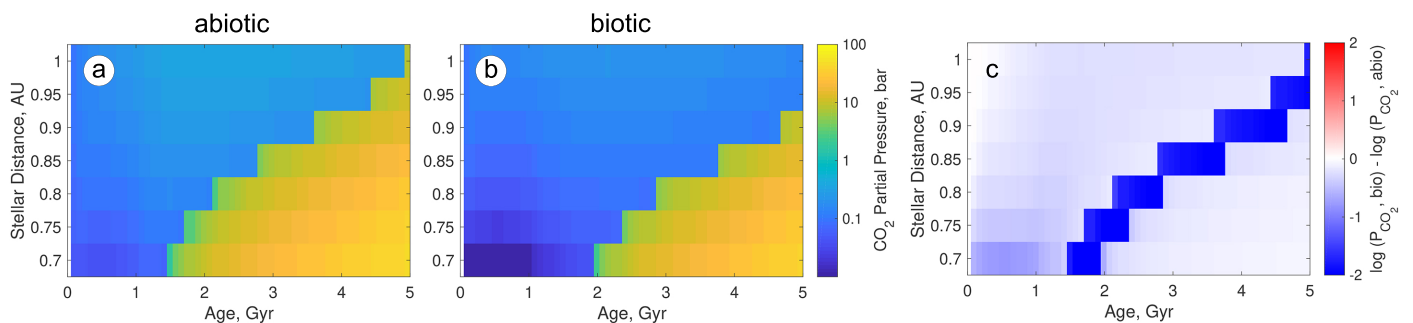


Fig. 1. Resulting atmospheric CO₂ from our interior-atmosphere model. We show model results of an abiotic planet (a), a biotic planet (b), and the difference between them (c). The planet parameters are $f_{O_2}=IW-0.2$, $T_0=1900$ K, and $\eta_{ref} = 10^{21}$ Pa s.

observed for large orbital distances (here: ≥ 0.9 AU; red region in Fig. 2f), which allow for a substantial increase in the crustal carbon concentration, and therefore of the rate of crustal decarbonation with time.

Another important parameter for stagnant-lid planets is the initial mantle temperature (e.g. Tosi et al. 2017; Noack et al. 2017; Dorn et al. 2018; Höning et al. 2019, 2021). In Fig. 2g–i, we explore the effect of initial mantle temperatures of 1850 K and 1950 K (baseline model: 1900 K). A high initial mantle temperature causes rapid early outgassing, implying a higher level of atmospheric CO₂ during the subsequent evolution. Ultimately, this affects the inner boundary of the habitable zone: the higher the initial mantle temperature, the earlier the runaway greenhouse sets in. We find that the biosphere in both cases has a substantial effect on the habitable timespan, particularly striking for the lower initial mantle temperature.

Finally, another controlling parameter in planetary evolution models is the mantle viscosity, which depends on the planet’s composition. Assuming a pressure- and temperature dependent viscosity following Grasset & Parmentier (1998) and Choblet & Sotin (2000), for our baseline model we set the reference viscosity to $\eta_{ref} = 10^{21}$ Pa s. In Fig. 2g–i, we additionally tested reference mantle viscosities of 10^{20} and 10^{22} Pa s. We find that a lower reference mantle viscosity substantially shortens the habitable timespan. This is a natural outcome of the more vigorous mantle convection, implying higher rates of outgassing particularly during the early evolution. Even a stellar distance of 1 AU does only allow for a habitable timespan of 2 Gyr. CO₂ accumulates rapidly and almost undiminished in the atmosphere, quickly making the surface conditions uninhabitable. We also observe that the impact of the biosphere is very limited in this case (extending the habitable timespan by only about 100 Myr). This is due to the fast circulation time of carbonates until they reach the decarbonation depth, which again is a result of the rapid mantle convection.

A main reason for the varying degree of influence of the effect of the biosphere on the habitable timespan is the trade-off between the biologically enhanced rate of weathering (enhancing carbon removal from the atmosphere) and the indirectly enhanced rate of crustal decarbonation (supplying CO₂ to the atmosphere). Importantly, this trade-off is controlled by the accumulated mass of carbon that has been stored in the crust throughout the planet’s history: the rate of crustal decarbonation depends on the integrated rate of – biologically enhanced – weathering. In Fig. 3, we depict this trade-off between mantle degassing, weathering and decarbonation (top panels: abiotic, bottom panels: biotic). We illustrate the cases for a mantle oxygen fugacity of IW+0 and orbital distances of 0.9 AU (Fig. 3, left panels) and 0.75 AU (Fig. 3, right panels), representing two specific cases

where the presence of the biosphere reduces (left panels) and extends (right panels) the habitable timespan of the planet.

During the first ≈ 1 Gyr, crustal decarbonation (blue) is zero and mantle carbon degassing (red) is fully compensated by weathering (yellow) for all planets. Subsequently, crustal decarbonation sets in, and the combined atmospheric carbon source fluxes (mantle degassing plus crustal decarbonation) are compensated by weathering. Depending on the stellar distance and on the presence of a biosphere, surface water evaporates between ≈ 1.5 Gyr (panel b) and 2.4 Gyr (panel a). Weathering ceases, CO₂ rapidly accumulates in the atmosphere, surface temperature rises, and crustal decarbonation speeds up. The sharp negative peaks of the yellow curves in panels a and b are of numerical origin. After the runaway greenhouse, the rate of mantle degassing increases due to the high surface temperature, which causes thinning of the stagnant lid and shallower melting.

A striking effect of the rate of biologically enhanced weathering is on the surface temperature. While for the abiotic planet (Fig. 3, top) the surface temperature rises strongly with time and more or less evenly until reaching $\approx 80^\circ\text{C}$ (followed by the onset of the runaway greenhouse), the rise of the surface temperature of the biotic planet (Fig. 3, bottom) is slowed down by the temperature-dependence of the biological productivity. Therefore, the biotic planet maintains a moderate surface temperature ($\lesssim 35^\circ\text{C}$) for almost the entire habitable period, which is followed by a dramatic temperature rise as the bioproductivity becomes less effective at higher temperatures (compare Eq. 4) and ultimately by the transition into the runaway-greenhouse regime.

3.2. Observational signatures of bioproductivity

In section 3.1, we demonstrated that the atmospheric CO₂ concentration of a planet near the inner edge of the habitable zone depends on whether the planet is inhabited. Under the condition that other planet-specific parameters could be inferred with sufficient accuracy, this finding presents an intriguing potential observable for future space telescopes.

In the following, we study features in the atmospheric spectrum indicating whether or not the planet underwent a runaway greenhouse in its history, which in turn depends on the presence or absence of a biosphere. We again used our baseline planet (Fig. 1) and a stellar distance of 0.9 AU. We illustrate the spectra for the abiotic and biotic planet for two points in time: at 3 Gyr and 4 Gyr. These parameter combinations are well suited for illustration purposes as they cover the transition (both the abiotic and biotic planet are habitable at 3 Gyr, but only the biotic planet is habitable at 4 Gyr).

We used the atmosphere biochemistry model 1D-TERRA for the biotic scenarios to explore the impact of bioproductivity on

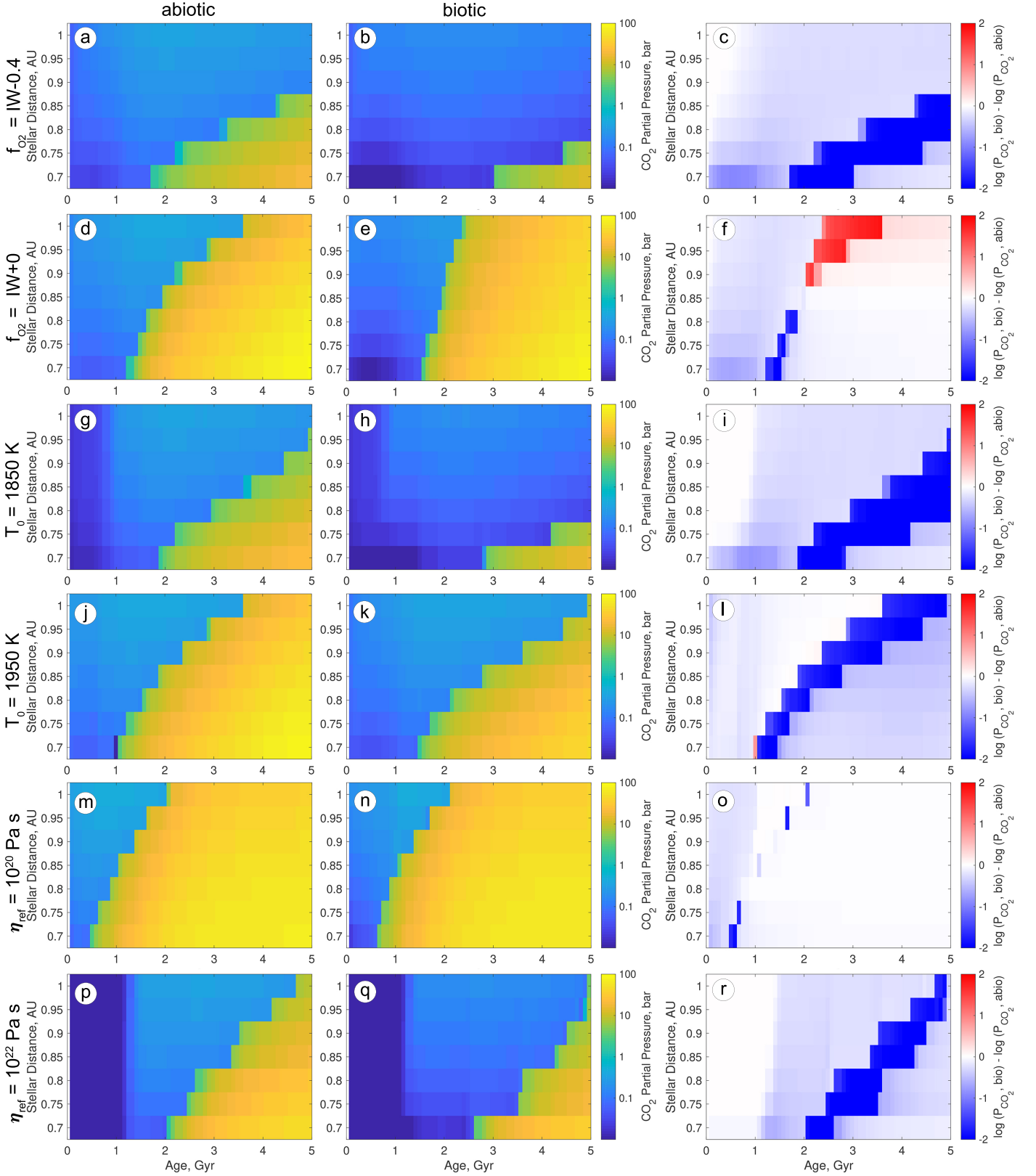


Fig. 2. Atmospheric CO_2 of an abiotic planet (left column), a biotic planet (centre column), and the difference between the two (right column). We tested different oxygen fugacities f_{O_2} (a–f), initial mantle temperatures T_0 (g–l), and reference mantle viscosities η_{ref} (m–r) keeping the respective other parameters equal to the baseline model ($f_{O_2} = IW-0.2$, $T_0 = 1900$ K, $\eta_{ref} = 10^{21}$ Pa s).

atmospheric CH_4 and on the hydrological cycle as CO_2 and thus water vapour increase. In order to cover uncertainties related to modelling the hydrological cycle, we calculated two versions for the biotic scenarios 1&2 with 1D-TERRA (section D): the dry

version reflects an efficient hydrological cycle with the majority of the water vapour already condensing near the surface – similar to current Earth, whereas the moist version reflects a scenario in which a significant water fraction diffuses into the stratosphere.

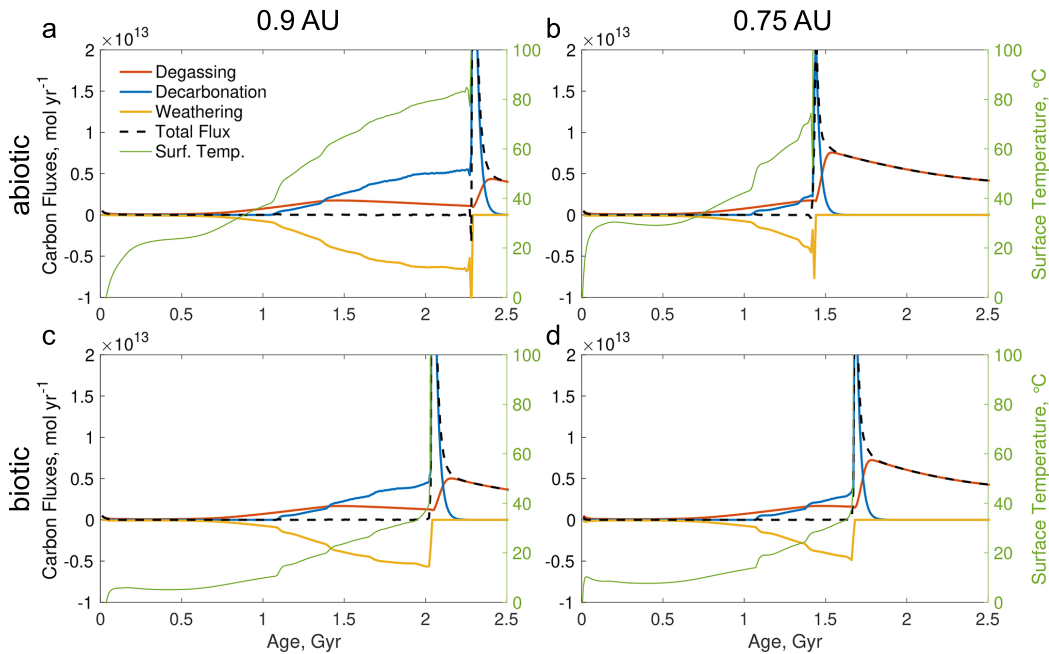


Fig. 3. Interior-atmosphere carbon fluxes and surface temperature. We used a mantle oxidation state of IW+0 and a stellar distance of $d=0.9$ AU (left) and 0.75 AU (right) for an abiotic planet (top) and for a biotic planet (bottom). We show mantle carbon degassing (red), crustal decarbonation (blue), weathering (yellow), combined carbon fluxes (black), and surface temperature (green, right axes).

Table 3. Scenarios to model the atmospheric spectra.

Scenario	Description	Insolation	P_{CO_2} [bar]	P_{H_2O} [bar]	x_{H_2O}
Dry 1	Biotic, 3 Gyr	1481.2 W m^{-2}	$1.366 \cdot 10^{-1}$ bar	$4.333 \cdot 10^{-2}$ bar	$\sim 10^{-6}$ (a)
Moist 1	Biotic, 3 Gyr	1481.2 W m^{-2}	$1.366 \cdot 10^{-1}$ bar	$4.333 \cdot 10^{-2}$ bar	$10^{-1} - 10^{-5}$ (a)
Dry 2	Biotic, 4 Gyr	1602.2 W m^{-2}	$1.186 \cdot 10^{-1}$ bar	$4.968 \cdot 10^{-2}$ bar	$\sim 10^{-6}$ (a)
Moist 2	Biotic, 4 Gyr	1602.2 W m^{-2}	$1.186 \cdot 10^{-1}$ bar	$4.968 \cdot 10^{-2}$ bar	$10^{-1} - 10^{-5}$ (a)
Steam 3	Abiotic, 3 Gyr	1481.2 W m^{-2}	$2.082 \cdot 10^{-1}$ bar	$3.755 \cdot 10^{-1}$ bar	23.7%
Steam 4	Abiotic, 4 Gyr	1602.2 W m^{-2}	8.513 bar	$2.715 \cdot 10^2$ bar	96.6%
Desiccated 4	Abiotic, 4 Gyr	1602.2 W m^{-2}	8.513 bar	0 bar	0%

Notes: x_{H_2O} is the water volume mixing ratio. (a) H_2O abundances in the atmosphere are modified by the assumed hydrological cycle. We note that the atmosphere model 1D TERRA starts 0.5 km above the modelling domain of the geophysical model (see Section E). For all scenarios, we assumed an oxygen fugacity of IW-0.2 and an orbital distance of 0.9 AU from a Sun-like star. We assumed a background gas for all models of 1 bar N_2 and for the biotic model runs additionally 0.2 bar O_2 .

The moist scenario is thus directly motivated by the outcome of our geophysical model evolution model (see also Appendix E). Furthermore, for a general overview of the two scenarios, the reader is referred to Table 3. For an overview of the model 1D-TERRA (Wunderlich et al. 2020), the reader is referred to Appendix D. We note that our moist scenario yields a much higher humidity (by about a factor of 100 in volume mixing ratio) at the near-surface level than the ‘wet’ scenario investigated in Wunderlich et al. (2020).

Figure 4 shows that the dry scenarios 1 and 2 yield similar results with an ozone driven temperature inversion in the stratosphere. Here, the buffering effect of biological enhanced weathering is very strong, keeping the planet habitable despite higher irradiation. Conversely, the moist scenarios 1 and 2 show higher surface temperatures compared to the dry models due to larger amount of H_2O vapour in the atmosphere, which is an efficient greenhouse gas. For the moist scenario 2, the surface may become even too hot to remain habitable. In addition, the higher moistness of the stratosphere diminishes the stratosphere temperature inversion (moist scenario 1) or can even remove it

entirely (moist scenario 2) such that the stratosphere becomes cooler compared to the dry biotic scenarios.

In the moist scenarios, the abundance of H_2O in the atmosphere is larger by at least one order of magnitude compared to the dry scenarios and is particularly high for the lower troposphere ($p > 0.1$ bar). Consequently, CH_4 is diminished by reactions with OH-radicals in the moist scenarios near the surface. The effect is strongest for the moist scenario 2, for which very high water volume mixing ratios (VMR) > 0.1 lead to a very high destruction rate by several orders of magnitude for CH_4 . In comparison, the CH_4 volume mixing ratios produced by the biomass in the moist scenario 1 are only diminished by one order of magnitude compared to the dry, biotic cases that retain relatively high methane abundances of 2×10^6 throughout the atmosphere. We note that CO_2 abundances set near the surface via surface weathering are approximately constant throughout the atmosphere. As noted above, our moist scenarios are 100 times more humid than the wet scenarios in Wunderlich et al. (2020), who therefore could not capture the destruction of CH_4 , which we do observe.

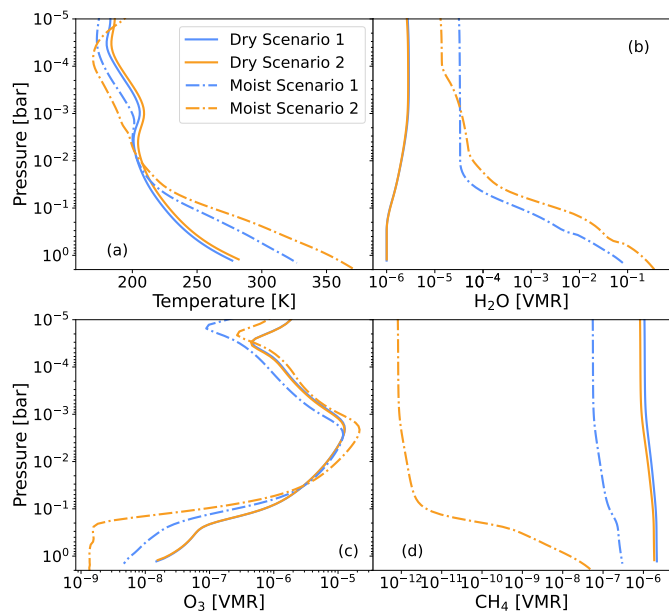


Fig. 4. Model results from 1D-TERRA. We show (a) pressure-temperature profiles with efficient near surface condensation and (b–d) abundances or volume mixing ratios (VMR) for (b) H₂O, (c) O₃, and (d) CH₄. The biotic scenarios 1 and 2 are shown in blue and orange, respectively, dry scenarios are denoted by solid lines and moist scenarios by dashed-dotted lines.

Similar to CH₄, the abundances of ozone are diminished in the lower troposphere ($p < 0.1$ bar) with increasing water vapour abundances. However, the majority of O₃ is photochemically created at higher altitudes, where water abundances are relatively low ($< 10^{-4}$) even for the moist scenarios and the latter do not strongly affect O₃ abundances. The gradual disappearance of the stratospheric temperature inversion with increasing atmosphere moisture is solely due to the latent heat release of water vapour condensing out of the atmosphere, which is stronger than the radiative heating by ozone.

The chemistry results from 1D-TERRA suggest that ozone remains a robust biosignature and that CH₄ abundances can remain high unless water vapour abundances exceed more than 10% in the lower troposphere. This does, however, not necessarily mean that these two molecules can be detected with JWST on a rocky exoplanet at the inner edge of the host star’s habitable zone like TRAPPIST-1e. To explore the observability of the biotic scenarios 1 and 2 with JWST/NIRSpec and JWST/MIRI, we used the abundances and pressure-temperature profiles from 1D-TERRA (Wunderlich et al. 2020) as input parameters for the radiative transfer calculations with `petitRADTRANS` (Mollière et al. 2019) and opacity sources with N₂ pressure broadening ($p_{N_2} = 1$ bar) and added continuum as listed in Table A.1. To calculate the noise in the respective JWST observation modes, we employed PANDEXO (Batalha et al. 2017) and applied the scenarios to TRAPPIST-1e that lies at the inner edge of the habitable zone of its host star. For clarity, we focus on the most promising scenario to detect biosignatures: the dry, biotic scenarios 1 & 2.

If 100 transit observations are invested, then the strong CO₂ line can be well resolved with JWST/NIRSpec for TRAPPIST-1e, where we find an accuracy of 10 ppm for 100 transits, which is more conservative than the results of Lustig-Yaeger et al. (2022) who derived even better accuracy of 7–8 pm in the 3–5 micron range (Figure 5). Conversely, the narrow O₃ biosignature is the strongest for the dry scenarios at 3.27 micron in the

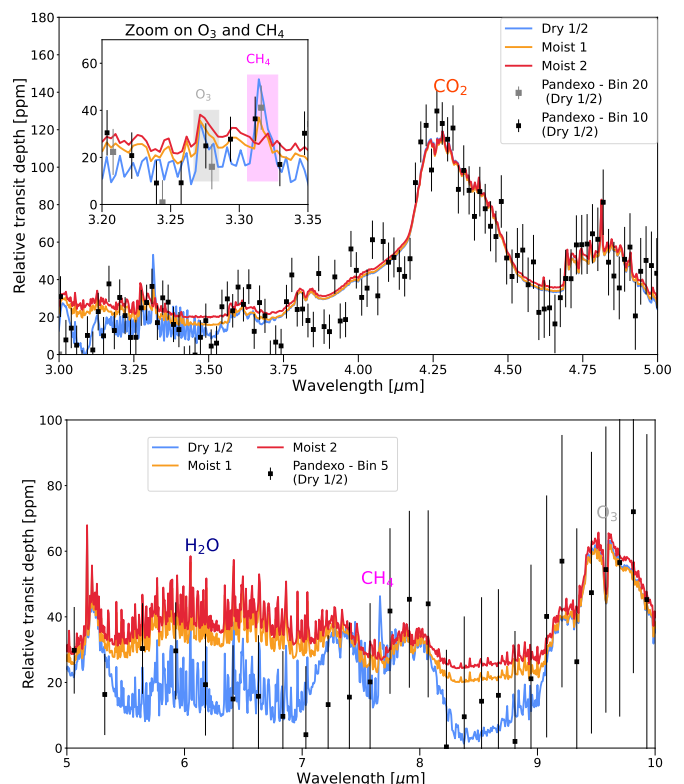


Fig. 5. Transmission spectra for the dry and moist biotic scenarios 1 & 2. We show the JWST/NIRSpec range between 3–5 micron (top) with an inlay for the 3.2–3.35 micron range to highlight the O₃ (grey box) and CH₄ feature (magenta box). The bottom panel shows transmission spectra for 5–10 micron in the JWST/MIRI range (bottom). We note that the transmission spectra for the dry biotic scenarios 1 and 2 are identical. We further simulated JWST observations with PANDEXO for one scenario (dry 1/2) with 100 transit observations of TRAPPIST-1e (black error bars). We chose the G395M grism setting with 10 pixels per bin (top), 10 and 20 pixels per bins (inlay), and MIRI LRS setting with 5 pixels per bin (bottom panel).

NIRSpec range and 9.8 micron in the MIRI range. In the NIRSpec range, the O₃ signal is very narrow and lies just left of the stronger CH₄ signature. In the JWST/MIRI range, the CH₄ and O₃ signatures are broader and farther apart. Unfortunately, even with 100 JWST observations, we estimate an accuracy of 20 ppm for JWST/MIRI and thus both the O₃ and CH₄ spectroscopic feature amplitudes are only at 1σ in the cloud-free case. Investing 100 transit observations using MIRI with its lower data accuracy does therefore not appear to be promising to identify the signatures of the biotic atmosphere scenarios.

A close-up of the O₃–CH₄ double feature in the NIRSpec range (Figure 5, inlay) clearly shows that O₃ has a signal strength between 1–2 σ for all scenarios. The higher bioproductivity of scenarios 1 and 2 (see Appendix D) lead, however, to a relatively high CH₄ signature of 40 ppm for the dry scenarios that is well above 3σ with 100 JWST observations when neglecting the impact of clouds. However, achieving an accuracy of 10 ppm with the observational data requires reducing the wavelength resolution down to 10–20 pixels per bin, which resolves the CH₄ signal with only 1–2 points. With increasing water vapour content in the atmosphere, however, CH₄ will be destroyed near the surface and the signal drops to 1σ already for the moist scenario 1. For even more water vapour, CH₄ is not observable.

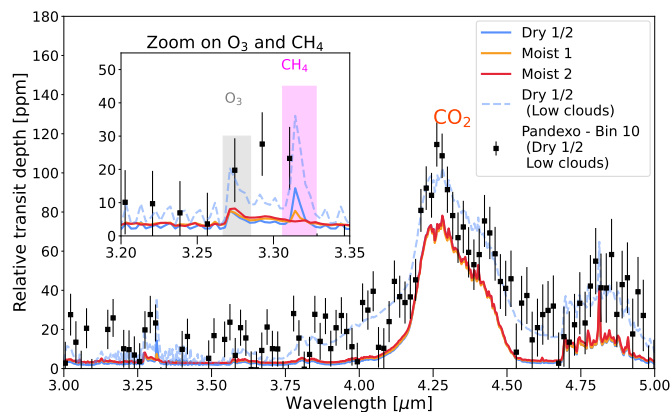


Fig. 6. Transmission spectra for the biotic scenarios. We show the JWST/NIRSpec range between 3 – 5 micron with a continuous grey cloud deck at the $p = 0.01$ bar (solid lines) and the dry biotic scenarios 1 & 2 with a lower cloud deck at the $p = 0.1$ bar (dashed line). The inlay for the 3.2 – 3.35 micron range highlights the O₃ (grey box) and CH₄ feature (magenta box). We further simulated JWST observations with PANDEXO for the dry biotic scenarios 1 & 2 with the lower cloud deck, simulating 100 transit observations of TRAPPIST-1e (black error bars). We chose the G395M grism setting and combined 10 pixels in one bin.

We further tested the impact of clouds on the biosignatures for the NIRSpec transmission spectra, which appears to be most promising to identify a habitable, biotic planet with JWST. Such observations will support statistical studies of the extension of the habitable zone (Lehmer et al. 2020; Schlecker et al. 2024). We first assumed a grey cloud deck at $p = 10^{-2}$ bar. This scenario is roughly equivalent to a thick tropical cumulonimbus thundercloud and therefore represents the worst case scenario for a dry Earth-like atmosphere. Figure 6 shows that the CH₄ signal strength that was found to be above 3σ in the cloud-free, dry scenario for 100 JWST observations drops down to 10 ppm or 1σ with thick thundercloud coverage. The O₃ signature at 3.3 micron remains visible because the majority of the ozone layer is well above the cloud top (Figure 4). The amplitude of the ozone line is, however, diminished by a factor of two and is thus below 1σ with 100 transit observations for a cloudy atmosphere.

We also tested a more benign case with a cloud top at 0.1 bar for the dry biotic scenarios, which would correspond to a thinner stratocumulus cloud for an Earth-like atmosphere. Here, the CH₄ signature drops from 40 ppm to 30 ppm, which is still at 3σ even with our conservative noise estimate for 100 JWST observations. Again, the necessary reduction in wavelength resolution to achieve 10 ppm accuracy leaves at most 2 points to resolve the CH₄ signature.

For all cloud scenarios, the amplitude of the CO₂ feature remains well above 3σ even in this thick cloud case and should thus allow to constrain the state of the silicate weathering cycle as outlined by Lustig-Yaeger et al. (2022). The 4.25 micron CO₂ feature ($P_{CO_2} = (1.196 - 1.366) \cdot 10^{-1}$ bar) appears to be very robust against changes in water vapour abundances and pressure-temperature profile variations of up to 100 K at the surface. It is clearly identifiable with 100 transit measurements even with a relatively high cloud deck. The 4.25 micron CO₂ feature can thus be seen as a reliable indicator of CO₂ abundances (see also Lustig-Yaeger et al. 2022).

Given the large time investment that is needed to characterise atmospheres of rocky planets, we also explored signatures of other atmosphere scenarios that signal the end of habitability.

To this aim, we constructed two scenarios with surface temperatures that are too high to sustain habitability and that would also result in total failure of the hydrological cycle (steam-dominated atmosphere scenarios 3&4). A steam-dominated atmosphere is, however, expected to result in a desiccated CO₂-dominated atmosphere within 100 million years (see also Table 3). These scenarios are explored as supplemental information in the Appendix (A, B and C).

4. Discussion

How does biological enhancement of weathering affect the habitable timespan of exoplanets? Could we use this insight to advance the search for life beyond Earth? To answer these questions, we modelled the coupled interior-atmosphere evolution of stagnant-lid planets accounting for biologically enhanced weathering and compared the evolution of the atmospheric CO₂ partial pressure between a biotic and an abiotic planet for different planet compositions and orbital distances. Following this, we compared the resulting emission and transmission spectra between these planets.

4.1. Impact of bioproductivity and other planet-specific parameters on atmospheric CO₂

Our results indicate that the biosphere has the potential to significantly extend the habitable period. For planets located near the inner edge of the habitable zone, with similar planet parameters (such as interior composition), the CO₂ signature of inhabited planets with active weathering would be distinguishable from that of abiotic planets that have undergone a runaway-greenhouse effect. However, it is important to note that our results are based on forward modelling with specific, well-defined input parameters. In particular, mantle oxygen fugacity, initial mantle temperature, and reference mantle viscosity play crucial roles. If the atmospheric CO₂ signature of an exoplanet is observed without information about these parameters, it is not possible to directly link the CO₂ signature to the presence or absence of a biosphere. Improved constraints on these parameters will help resolve this ambiguity, which we address in the following.

Inferring the mantle oxygen fugacity of exoplanets with sufficient accuracy is a primary challenge in isolating the effect of life on the habitable timespan. While a biosphere for a moderately reduced mantle (IW-0.4) substantially extends the habitable timespan across all explored stellar distances, for a more oxidised mantle (IW+0), the biosphere extends the habitable timespan only for planets close to their host star and only to a limited extent. This suggests that planets with high incident insolation are the most suited to a use biologically prolonged habitable period as a biosignature.

One way to infer a planet's oxidation state is by analysing the observed ratio between reduced species (CO, H₂) and oxidised species (CO₂, H₂O) (e.g. Ortenzi et al. 2020; Liggins et al. 2022). Another complementary approach is to study the planet's host star, as both the planet and the star are formed from the same primordial material (e.g. Adibekyan et al. 2021; Guimond et al. 2023). However, as pointed out by Guimond et al. (2023), even with the same Fe₃⁺/ΣFe ratio, the mantle oxidation state can vary significantly depending on its bulk composition. Finally, ongoing advancements in exoplanet atmosphere characterisation will further enhance our understanding of the diversity of mantle oxidation states (Ortenzi et al. 2020).

In addition to the mantle oxidation state, the initial mantle temperature and the reference mantle viscosity are impor-

tant abiotic factors that influence the habitable timespan of a stagnant-lid planet by controlling the early outgassing rate of CO₂. Planetary accretion models can provide insights into the initial thermal energy, and thus the initial mantle temperature, for planets in general (e.g. Schubert et al. 2001). In contrast, the reference mantle viscosity could vary between planets in particular due to differences in the volatile content in the mantle (e.g. Karato et al. 1986). Models of planetary system formation can offer insights into the bulk volatile concentration of exoplanets (e.g. Kamp et al. 2013; Moriarty et al. 2014), making them highly relevant in this context.

Parameter uncertainties explored in this study highlight the need for future research, particularly focused on refining our understanding of exoplanet composition and initial mantle temperature, to effectively use the biologically extended habitable period as a meaningful biomarker. Nevertheless, even if uncertainties related to abiotic factors remain difficult to reduce and may overshadow biosphere-related effects, the framework presented here provides a valuable approach for selecting the most promising exoplanets for follow-up studies: in particular, planets near the inner edge of the habitable zone with low atmospheric CO₂ levels are strong candidates to have an active biosphere. If planet-specific parameters can be inferred, exoplanets that meet these criteria and also have a reduced mantle ($\leq \text{IW-0.2}$) and high mantle viscosity ($\eta_{ref} \geq 10^{21}$ Pa s) should be prioritised for future long-term observations, as the influence of a biosphere in prolonging the habitable period is especially pronounced under these conditions. While we found that the initial mantle temperature can shift the habitable timespan, its influence on the impact of a biosphere is minimal.

From the biological point of view, a main simplification of our model was that even though we calculated the bioproductivity as a function of temperature and atmospheric CO₂ concentration, we neglected any temporal biological evolution. On Earth, land plants, which substantially enhance weathering, have emerged only in the Paleozoic (Berner 1997). If this also applies to the stagnant-lid planets discussed in this paper, the early period (until the emergence of land plants) of the biotic planet would resemble that of the abiotic planet and so would the crustal carbon concentration. If land plants emerged later, shortly before the planet would otherwise become too hot, biologically-enhanced weathering would efficiently extend the habitable timespan since the decarbonation rate would follow the weathering rate with a delay: it takes time until carbonated crust reaches the decarbonation depth, at least about 1 Gyr, and even more in the later evolution, due to the cooler mantle and hence the smaller rate of crustal production (compare Höning et al. 2019). We also note that the assumed factor of biological enhancement of weathering on present-day Earth is a conservative estimate; an abiotic Earth would likely have an even smaller reference weathering rate (Lenton et al. 2018).

4.2. Observability of the signatures of bioproductivity

Several studies have explored the observability of CO₂ and biosignatures like CH₄ and O₃ under conditions of increased irradiation compared to present-day Earth (Schwieterman et al. 2019; Wunderlich et al. 2020; Lustig-Yaeger et al. 2022). These studies, however, relied on assumptions on methane production based on present-day Earth rates, treated it as a free parameter, and/or did not consider the interplay between the biosphere and atmospheric CO₂. Wunderlich et al. (2020) investigated the impact of increased humidity on CH₄ and O₃ due to changes in the water cycle, but without considering feedback with the bio-

Table 4. Overview of biosignature production.

	CH ₄ flux [cm ⁻² /s]	CO ₂ [bar]
Scenario 1	$1.25 \cdot 10^{11}$	$1.366 \cdot 10^{-1}$
Scenario 2	$1.14 \cdot 10^{11}$	$1.186 \cdot 10^{-1}$
W2020	$6.31 \cdot 10^{10}, 1.12 \cdot 10^8$	10^{-1}
S2019	$10^6 - 10^{14}$	$4 \cdot 10^{-2}$

Notes: W2020: Wunderlich et al. (2020); S2019: Schwieterman et al. (2019). The O₂ flux is $1.21 \cdot 10^{12}$ cm⁻²/s in all cases. The CH₄ flux used by Wunderlich et al. (2020) is the biotically generated flux for present-day Earth without anthropogenic contributions.

sphere. Table 4 summarises methane, oxygen fluxes and CO₂ from studies most similar to this work. In our study, we derived the biotic CH₄ production rate from the coupled model. Furthermore, we made two extreme humidity assumptions for the atmosphere above the atmospheric planetary boundary layer, which can be seen as the interface region between the geophysical and the atmospheric model employed here (see sections D and E). We found that the humidity has a strong impact on the atmospheric CH₄ levels and a less pronounced impact on atmospheric O₃. We also assessed the impact of clouds, identifying scenarios where cloud cover could diminish the observability of CH₄.

Our results show that the CO₂ absorption band at 4.3 micron is well resolvable with 100 transit observations with JWST/NIRSpec. This is in accordance with Lustig-Yaeger et al. (2022), who studied the potential observability of habitability of TRAPPIST-1e. Between 3.2 and 3.4 micron, O₃ and CH₄ features, in principle, allow to identify the habitable, biotic scenarios 1&2. However, only the CH₄ signature arising from the increased bioactivity reaches $\approx 3\sigma$ significance. This holds even true in the presence of a low cloud deck at 0.1 bar. Reaching the necessary 10 ppm accuracy to identify CH₄ requires, however, data binning down to 1–2 points in the narrow CH₄ (3.30 μm and 3.35 μm) absorption feature. Thus, a robust CH₄ detection will require careful treatment of systematic and stellar noise.

We stress that we chose conservatively that the noise accuracy is not higher than 10 ppm between 3–4 μm . Lustig-Yaeger et al. (2022), on the other hand, simulate an even higher accuracy (8 ppm) with 100 transit measurements in this critical wavelength range, which would raise the amplitude of the CH₄ signature to more than 4σ . We further point out a similarly challenging and successful detection in exoplanetary atmospheres: He was identified with HST/WFC3 observations with improved data and noise treatment based on a single, binned data point (Spake et al. 2018). Thus, we conclude that while identifying CH₄ with JWST/NIRSpec transit observations might be challenging, it is a worthwhile endeavour if we aim to identify habitable temperate worlds in the near future. With the prolonged habitability due to feedback with the biosphere, we also highlight that the period where CH₄ and O₃ is present in the atmosphere can be significantly extended.

Ostberg et al. (2023) also conclude that the 3.3 μm CH₄ atmospheric feature is ideally suited to identify a habitable Exo-Earth. The significance of the CH₄ biosignature drops, however, below 1σ in the presence of a thick continuous cloud deck at $p = 0.01$ bar. Further, if the water vapour content increases to 1%-10% at surface level, then OH radicals destroy CH₄¹.

¹ The importance of the OH production rate and the photochemical time scales for CH₄ is also pointed out by Wunderlich et al. (2020); Grenfell et al. (2013); Schwieterman et al. (2019).

Thus, the observability of biosignatures depends critically on an efficient hydrological cycle and cloud formation as the planet evolves out of habitability.

In our dry scenarios, the resulting CH₄ and O₃ amplitudes of 60 ppm and 40 ppm are roughly in agreement with the outcome of the most similar scenario with 0.1 bar CO₂ from Wunderlich et al. (2020), though that study did not account for instrumental noise and cloud effects. We found that, without efficient rainout, the geophysical evolution leads to higher humidity than in the wet model from Wunderlich et al. (2020). As a consequence, OH radical production becomes efficient enough to destroy CH₄, even in a low UV environment around M dwarfs, which generally favour methane preservation (Wunderlich et al. 2019; Schwieterman & Leung 2024). This effect arises once the water vapour volume mixing ratio at the bottom of the atmosphere model exceeds 0.1, which is more than 100 times larger than in the wettest conditions in Wunderlich et al. (2020). Additionally, we observe a sharp shift from CH₄-preservation to destruction in response to high H₂O levels, with atmospheric CH₄ abundances dropping by 6 orders of magnitude between moist scenarios 1 and scenario 2 as the water vapour mixing ratio increases from 0.1 – 0.2 at the bottom (Figure 4). Therefore, our work highlights that even around M dwarfs, CH₄ might be produced but could become unobservable in extremely humid atmospheres. In contrast, O₃ generated in the upper atmosphere remains relatively unaffected by increased atmospheric humidity. Therefore, constraining atmospheric water abundances along with the detection of O₃ or O₂ would be required to identify a moist biotic scenario.

The inferred O₃ abundances for the biotic scenarios 1 & 2 with 1D TERRA can reach $\approx 10^{-5}$ in the stratosphere, which is similar to Earth's current ozone concentration and also agrees with a recent 3D ozone chemistry model for tidally locked exo-Earths (Braam et al. 2022). For exo-Earths around M dwarf stars, however, a range of possible O₃ scenarios is discussed. On these tidally locked planets, O₃ distribution is highly affected by 3D circulation (e.g. Carone et al. 2018; Chen et al. 2019, 2021; Braam et al. 2022, 2023). Consequently, results for O₃ concentrations on Earth-like atmospheres around M dwarfs range between abundances smaller than one order of magnitude (Yates et al. 2020) or larger by two orders of magnitude compared to Earth with flare driven ozone production (Chen et al. 2021). The O₃ abundances found in this work would yield only a 2 σ O₃ signal at 3.2 micron with 100 JWST transit observations for TRAPPIST-1e, even in the cloud-free case. An enrichment by a factor of 100 in abundance may push the O₃ signal to detectable levels (Barstow & Irwin 2016). However, the O₃ absorption feature in the 3.27 μm is even narrower than the CH₄ feature (Fig. 5, inlay) and thus any attempt to detect O₃ with JWST/NIRSpec will similarly require highly accurate noise reduction.

Although O₃ may be difficult to observe with JWST, it is, in principle, a relatively stable indicator of biotic atmospheres in our model framework. It is photochemically produced above the cloud deck and its abundances are hardly affected by higher water abundances even in the case of a less efficient water cycle (moist biotic scenarios 1 & 2). In the case of a cloud-free habitable dayside or a dayside that is only partly covered by clouds, already 10 eclipse observations with JWST/MIRI could yield some insights. Here, the CH₄ biosignature at 7.7 micron (2 σ) and the O₃ signature at 9.5 micron (3 σ) do not overlap. However, in case of a continuous cloud deck at $p = 10^{-2}$ bar, the almost isothermal upper atmosphere will make the observation of molecular features impossible.

Snellen et al. (2013) point out that the identification of O₃ and O₂ on potentially habitable worlds could be challenging even with telescopes like the Extremely Large Telescope (ELT) due to telluric contamination. The identification of molecular O₂ in the optical, specifically in the 0.76 μm band, could be more promising. In this band, telluric oxygen could be differentiated from oxygen in the atmosphere of the observed planet. However, O₂ alone without the identification of H₂O, CO₂ and ideally also CH₄ is not a definitive biomarker for rocky planets around M dwarf stars, where efficient XUV photolysis of H₂O can easily create O₂ abiotically (Luger & Barnes 2015; Meadows et al. 2018). High resolution spectroscopy ($R \sim 100,000$) observations of O₂ with ground based telescopes like ELT may help, however, to distinguish between biotic and abiotic scenarios for rocky planets, for which H₂O and CO₂ has been found with space based telescopes. Spectrographs on space telescopes are typically limited in spectral resolution ($R < 10,000$) and thus not well suited to uniquely identifying the relative narrow O₂ lines (e.g. Lin & Kaltenegger 2022). Lin & Kaltenegger (2022), specifically, point out that the ELT combined with the JWST can be highly useful in assessing of habitability on TRAPPIST-1e.

Cloud coverage depends on the 3D climate state of the rocky planets. Tidally locked 3D exo-Earth scenarios for TRAPPIST-1e consistently predict a climate state with a strong upwelling branch over the dayside (e.g. Carone et al. 2018; Braam et al. 2022; Krissansen-Totton et al. 2022), where eclipse observations would probe. The resulting thick dayside clouds would render observations difficult and eclipse data would be consistent with a feature-less black body curve between 200 K and 320 K, depending on the upper atmosphere temperatures. The 200 K scenarios would be valid for the biotic, habitable scenarios but also for a desiccated CO₂ atmosphere after the planet has been rendered uninhabitable. The 320 K upper atmosphere scenarios are steam-dominated atmospheres or runaway-greenhouse atmosphere scenarios (e.g. Goldblatt et al. 2013; Schlecker et al. 2024; Barth et al. 2021; Boukrouche et al. 2021).

Clouds complicate the observability of rocky planets (e.g. Komacek et al. 2020; Ostberg et al. 2023; Cohen et al. 2024). We note, however, that the coverage of high-altitude hazes in biotic Earth-like atmospheres is not expected, because for such a scenario CH₄/CO₂ ratios greater than 1 would be required (Arney et al. 2016). For the desiccated scenario 4, we did not explore the impact of hazes further because the grey cloud deck scenario already renders such an atmosphere difficult to constrain. SO₂ as a signature of geophysical activity might be promising for exo-Venus identification (Ostberg et al. 2023).

Three-dimensional exo-Earth climate simulations for TRAPPIST-1e predict that the terminator regions, where transmission spectra probe, should be virtually cloud-free (Sergeev et al. 2022b). Thus, 100 JWST transit observations with NIRSpec are a worthwhile time investment to aim at constraining at least CO₂ and CH₄. This is true, in particular, since the 4.3 micron CO₂ absorption band remains a robust feature of oxidised exoplanet atmospheres also beyond habitable scenarios. If paired with constraints of H₂O signatures at shorter wavelengths (1 – 3 micron), JWST transmission observations may also help constrain the humidity of the planet's climate. This will require, however, an investment in minimising the impact of the strong variability of the host star (Rackham et al. 2023).

Despite all the observational challenges, observations of planets near the inner edge of the habitable zone like TRAPPIST-1e will pave the way to identify potentially biotic planets with a suitable range of CO₂ abundances, to re-assess the limits of the

habitable zone, and therefore to maximise our chances to characterise a habitable and potentially inhabited world in the near future. This requires, however, also to recognise moist biotic scenarios as outlined in this work.

We further point out that non-tidally locked rocky exoplanets, on which the space mission PLATO will focus, would potentially exhibit a non-continuous cloud coverage. The proposed LIFE mission is ideally suited to characterise these non-tidally locked planets in the habitable zone of FGK stars (Alej et al. 2022).

Last but not least, we stress that rocky exoplanet atmospheres are complex and that various effects may lead to similar observational signatures. The case of the temperate sub-Neptune K2-18b serves as an example that the atmospheres of temperate worlds can in principle be characterised and also acts as a cautionary tale. The recently obtained JWST observations of CH₄ and CO₂ in a reducing H₂-dominated atmosphere with a notable absence of H₂O call for disequilibrium chemistry models that connect deeper parts of the planet with the observable atmosphere (Madhusudhan et al. 2023). However, a magma ocean below the atmosphere and a liquid water layer both can explain the JWST observations (Shorttle et al. 2024). Similar results could also arise for temperate rocky planets. Thus, it remains important to determine the potential complexity of these planets with a diverse set of models. One important factor is the impact of a biosphere and potential observable signatures as discussed in this work.

5. Conclusions

This study is the first to directly link the atmospheric CO₂ signature of planets near the inner edge of the habitable zone to the presence or absence of a biosphere. Specifically, we find that planets with low atmospheric CO₂ in this region are more likely to be inhabited, as biological processes efficiently regulate CO₂ levels through enhanced weathering and thereby postpone the runaway greenhouse and the accompanying dramatic rise of atmospheric CO₂. To reach this conclusion, we modelled the coupled interior-atmosphere evolution of stagnant-lid planets, accounting for biologically enhanced weathering, carbonate burial, and decarbonation. The resulting abundances of atmospheric gases were then used to simulate the spectral signatures.

For most parameters explored in this study, the presence of a biosphere significantly prolongs the habitable period of a planet, by up to approximately two billion years. The transition to an uninhabitable state is marked by an increase in atmospheric CO₂ partial pressure by roughly two orders of magnitude. As a result, planets with similar geophysical characteristics and orbital distances would exhibit vastly different CO₂ levels depending on whether they are inhabited or not.

However, biological enhancement of weathering is not the only factor controlling the habitable timespan. Mantle oxygen fugacity, initial mantle temperature, and reference mantle viscosity also play crucial roles. Isolating the effect of a biosphere on the habitable timespan to use it as a biomarker remains challenging, as it requires narrowing down these planet-specific parameters for observed targets. Nevertheless, even if abiotic factors cannot be completely constrained and may obscure the biosphere's influence, the framework presented here still provides valuable insights for identifying the most promising candidates to have an active biosphere. These candidates could then be prioritised for future long-term space-telescope observations. In particular, planets near the inner edge of the habitable zone with low atmospheric CO₂ would be of first-order interest. Additionally, planets with a reduced mantle and a high mantle viscosity

are promising, as these conditions amplify the effect of a biosphere in extending the habitable period. Under these circumstances, low levels of atmospheric CO₂ are even more likely to indicate the presence of life.

From an observational perspective, CO₂ serves as a key signature of active surface weathering and dominates the atmospheric spectrum at 4.3 microns. This feature should be readily detectable with 100 JWST transmission measurements, even under cloudy conditions, provided that the atmosphere is oxidised enough to suppress high-altitude hazes (Arney et al. 2016). Additionally, increased bioproductivity could yield a detectable CH₄ biosignature at 3.3 micron. However, the observability of CH₄ may be hindered by an inefficient hydrological cycle that enriches the atmosphere with water vapour, as OH radicals can destroy CH₄. We also find that the destruction of CH₄ is triggered when the water vapour volume mixing ratio exceeds 0.1 near the surface. At lower values, CH₄ abundances remain at least at 0.5 ppm throughout the atmosphere and reach 2 ppm for the dry scenarios and increased bioactivity. O₃ levels are more stable, even in our moist biotic scenarios, and cloud presence does not significantly hinder the detectability of O₃. Detecting the latter is likely challenging with 100 transmission observations, but already ten eclipse observations could constrain both CH₄ and O₃, assuming the planet's dayside is partially cloud-free.

Tidally locked rocky exo-Earths are expected to have continuous dayside cloud coverage. Therefore, additional ground-based observations with high-resolution telescopes such as the ELT could complement space-based data, helping to identify biosignatures before the launch of the Habitable World Observatory (HWO). In the immediate future, resolving the 4.3 micron CO₂ feature and potentially H₂O using JWST transmission spectra of potentially habitable planets such as TRAPPIST-1e offers a promising pathway for atmosphere characterisation (see also Lustig-Yaeger et al. 2022).

In summary, the control of bioproductivity on the onset of the runaway greenhouse near the inner edge of the habitable zone in combination with the observational CO₂ signatures accompanying the transition from a habitable to an uninhabitable world, as well as the determination of atmospheric CH₄ and O₃ in conjunction with a monitoring of water abundances, are promising pieces of the puzzle aiming to assess whether or not an exoplanet is inhabited. Future work is needed both to improve our understanding of the geological and geochemical state of exoplanets and to advance the development of the next generation of space telescopes.

Acknowledgements. We thank Brad Foley for valuable comments on a previous version of this manuscript. L.C. acknowledges support by the DFG priority programme SP1833 'Building a habitable Earth' Grant CA 1795/3, the Royal Astronomical Society University Fellowship URF R1 211718 hosted by the University of St Andrews, and the European Union H2020-MSCA-ITN-2019 1136 under Grant Agreement no. 860470 (CHAMELEON). J.L.G and N.I thank the German Research Foundation (DFG) for financial support via the project The Influence of Cosmic Rays on Exoplanetary Atmospheric Biosignatures (Project number 282759267). KH acknowledges the FED-tWIN research program STELLA (Prf-2021-022), funded by the Belgian Science Policy Office (BELSPO). P.B. and N.T. acknowledge support from the DFG through the priority program SPP1992 'Exploring the Diversity of Extrasolar Planets', grant TO 704/3-1.

References

- Abe, Y., Abe-Ouchi, A., Sleep, N. H., & Zahnle, K. J. 2011, *Astrobiology*, 11, 443
- Adibekyan, V., Dorn, C., Sousa, S. G., et al. 2021, *Science*, 374, 330
- Alej, E., Konrad, B. S., Angerhausen, D., et al. 2022, *A&A*, 665, A106
- Anisman, L. O., Chubb, K. L., Elsey, J., et al. 2022, *JQSRT*, 278, 108013

- Arney, G., Domagal-Goldman, S. D., Meadows, V. S., et al. 2016, *Astrobiology*, 16, 873
- Baranov, Y., Lafferty, W., Ma, Q., & Tipping, R. 2008, *JQSRT*, 109, 2291
- Barstow, J. K. & Irwin, P. G. J. 2016, *MNRAS*, 461, L92
- Barth, P., Carone, L., Barnes, R., et al. 2021, *Astrobiology*, 21, 1325
- Batalha, N. E., Mandell, A., Pontoppidan, K., et al. 2017, *PASP*, 129, 064501
- Baumeister, P., Tosi, N., Brachmann, C., Grenfell, J. L., & Noack, L. 2023, *A&A*, 675, A122
- Bean, J. L., Abbot, D. S., & Kempton, E. M. R. 2017, *ApJ*, 841, L24
- Bergman, N. M., Lenton, T. M., & Watson, A. J. 2004, *AJS*, 304, 397
- Berner, R. A. 1992, *GCA*, 56, 3225
- Berner, R. A. 1997, *Science*, 276, 544
- Boukrouche, R., Lichtenberg, T., & Pierrehumbert, R. T. 2021, *ApJ*, 919, 130
- Braam, M., Palmer, P. I., Decin, L., Cohen, M., & Mayne, N. J. 2023, *MNRAS*, 526, 263
- Braam, M., Palmer, P. I., Decin, L., et al. 2022, *MNRAS*, 517, 2383
- Brugger, B., Mousis, O., Deleuil, M., & Deschamps, F. 2017, *ApJ*, 850, 93
- Burkholder, J., Sander, S., Abbott, J., et al. 2015, *Chemical Kinetics and Photochemical Data for Use in Atmospheric Studies, Evaluation No. 18*
- Caldeira, K. & Kasting, J. F. 1992, *Nature*, 360, 721
- Carone, L., Keppens, R., & Decin, L. 2016, *MNRAS*, 461, 1981
- Carone, L., Keppens, R., Decin, L., & Henning, T. 2018, *MNRAS*, 473, 4672
- Catling, D. & Kasting, J. 2017, *Atmospheric Evolution on Inhabited and Lifeless Worlds* (Cambridge University Press)
- Chen, H., Wolf, E. T., Zhan, Z., & Horton, D. E. 2019, *ApJ*, 886, 16
- Chen, H., Zhan, Z., Youngblood, A., et al. 2021, *Nat. Astron.*, 5, 298
- Choblet, G. & Sotin, C. 2000, *PEPI*, 119, 321
- Cimino, J. 1982, *Icarus*, 51, 334
- Cohen, M., Palmer, P. I., Paradise, A., Bolasina, M. A., & Tiranti, P. I. 2024, *AJ*, 167, 97
- Davaille, A. & Jaupart, C. 1993, *J. Fluid Mech.*, 253, 141
- Dorn, C., Khan, A., Heng, K., et al. 2015, *A&A*, 577, A83
- Dorn, C., Noack, L., & Rozel, A. 2018, *A&A*, 614, A18
- Doyle, A. E., Young, E. D., Klein, B., Zuckerman, B., & Schlichting, H. E. 2019, *Science*, 366, 356
- Faucher, T. J., Turbet, M., Villanueva, G. L., et al. 2019, *ApJ*, 887, 194
- Foley, B. J. 2015, *ApJ*, 812, 36
- Foley, B. J. & Smye, A. J. 2018, *Astrobiology*, 18, 873
- Gaillard, F., Bouhifd, M. A., Füre, E., et al. 2021, *Space Sci. Rev.*, 217, 22
- Gebauer, S., Grenfell, J. L., Lehmann, R., & Rauer, H. 2018, *Astrobiology*, 18, 856
- Gialluca, M. T., Robinson, T. D., Rugheimer, S., & Wunderlich, F. 2021, *PASP*, 133, 054401
- Godolt, M., Grenfell, J. L., Kitzmann, D., et al. 2016, *A&A*, 592, A36
- Godolt, M., Tosi, N., Stracke, B., et al. 2019, *A&A*, 625, A12
- Goldblatt, C., Robinson, T. D., Zahnle, K. J., & Crisp, D. 2013, *Nature Geoscience*, 6, 661
- Gordon, I. E., Rothman, L. S., Hargreaves, R. J., et al. 2022, *J. Quant. Spectr. Rad. Transf.*, 277, 107949
- Gordon, I. E., Rothman, L. S., Hill, C., et al. 2017, *J. Quant. Spectr. Rad. Transf.*, 203, 3
- Graham, R. J., Lichtenberg, T., Boukrouche, R., & Pierrehumbert, R. T. 2021, *PSJ*, 2, 207
- Graham, R. J. & Pierrehumbert, R. 2020, *ApJ*, 896, 115
- Grasset, O. & Parmentier, E. M. 1998, *J. Geophys. Res.*, 103, 18171
- Grenfell, J. L., Gebauer, S., Godolt, M., et al. 2013, *Astrobiology*, 13, 415
- Gronoff, G., Arras, P., Baraka, S., et al. 2020, *JGR Space Physics*, 125, e27639
- Grott, M., Morschhauser, A., Breuer, D., & Hauber, E. 2011, *EPSL*, 308, 391
- Guimond, C. M., Shorttle, O., Jordan, S., & Rudge, J. F. 2023, *MNRAS*, 525, 3703
- Hamano, K., Abe, Y., & Genda, H. 2013, *Nature*, 497, 607
- Höning, D. 2020, *G3*, 21, e2020GC009105
- Höning, D., Baumeister, P., Grenfell, J. L., Tosi, N., & Way, M. J. 2021, *JGR Planets*, 126, e2021JE006895
- Höning, D., Tosi, N., & Spohn, T. 2019, *A&A*, 627, A48
- Janssen, L. J., Woitke, P., Herborn, O., et al. 2023, *Astron. Nachr.*, 344, e20230075
- Jenkins, J. M., Steffes, P. G., Hinson, D. P., Twicken, J. D., & Tyler, G. L. 1994, *Icarus*, 110, 79
- Kamp, I., Thi, W.-F., Meeus, G., et al. 2013, *A&A*, 559, A24
- Karato, S.-I., Paterson, M. S., & FitzGerald, J. D. 1986, *JGR Solid Earth*, 91, 8151
- Kasting, J. F. 1988, *Icarus*, 74, 472
- Kasting, J. F. & Catling, D. 2003, *ARA&A*, 41, 429
- Katz, R. F., Spiegelman, M., & Langmuir, C. H. 2003, *G3*, 4, 1073
- Komacek, T. D., Faucher, T. J., Wolf, E. T., & Abbot, D. S. 2020, *ApJ*, 888, L20
- Kopparapu, R. K., Ramirez, R., Kasting, J. F., et al. 2013, *ApJ*, 765, 131
- Krissansen-Totton, J. & Catling, D. C. 2017, *Nature Comm.*, 8, 15423
- Krissansen-Totton, J., Thompson, M., Galloway, M. L., & Fortney, J. J. 2022, *Nat. Astron.*, 6, 189
- Kruijver, A., Höning, D., & van Westrenen, W. 2021, *PSJ*, 2, 208
- Lehmer, O. R., Catling, D. C., & Krissansen-Totton, J. 2020, *Nature Comm.*, 11, 6153
- Lenton, T. M., Daines, S. J., & Mills, B. J. 2018, *ESR*, 178, 1
- Lenton, T. M. & von Bloh, W. 2001, *GRL*, 28, 1715
- Lichtenberg, T., Bower, D. J., Hammond, M., et al. 2021, *JGR Planets*, 126, e06711
- Liggins, P., Jordan, S., Rimmer, P. B., & Shorttle, O. 2022, *JGR Planets*, 127, e2021JE007123
- Lim, O., Benneke, B., Doyon, R., et al. 2023, *ApJ*, 955, L22
- Lin, Z. & Kaltenecker, L. 2022, *MNRAS*, 516, 3167
- Lincowski, A. P., Meadows, V. S., Zieba, S., et al. 2023, *ApJ*, 955, L7
- Luger, R. & Barnes, R. 2015, *Astrobiology*, 15, 119
- Lustig-Yaeger, J., Sotzen, K. S., Stevenson, K. B., et al. 2022, *AJ*, 163, 140
- Madhusudhan, N., Sarkar, S., Constantinou, S., et al. 2023, *ApJ*, 956, L13
- Mallard, W., Westley, F., Herron, J., Hampson, R., & Frizzell, D. 1994, *NIST Chemical Kinetics Database, version 6.0*
- Manabe, S. & Wetherald, R. T. 1967, *JAS*, 24, 241
- Meadows, V. S., Reinhard, C. T., Arney, G. N., et al. 2018, *Astrobiology*, 18, 630
- Mills, B., Daines, S. J., & Lenton, T. M. 2014, *G3*, 15, 4866
- Mlawer, E. J., Payne, V. H., Moncet, J.-L., et al. 2012, *PTRSA*, 370, 2520
- Mollière, P., Wardenier, J. P., van Boekel, R., et al. 2019, *A&A*, 627, A67
- Moresi, L.-N. & Solomatov, V. 1995, *Phys. Fluids*, 7, 2154
- Moriarty, J., Madhusudhan, N., & Fischer, D. 2014, *ApJ*, 787, 81
- Noack, L., Rivoldini, A., & Van Hoolst, T. 2017, *PEPI*, 269, 40
- Odintsova, T. A., Tretyakov, M. Y., Simonova, A. A., et al. 2020, *JMS*, 1210, 128046
- Ogawa, M., Schubert, G., & Zebib, A. 1991, *J. Fluid Mech.*, 233, 299
- Oosterloo, M., Höning, D., Kamp, I., & Van Der Tak, F. 2021, *A&A*, 649, A15
- Ortzeni, G., Noack, L., Sohl, F., et al. 2020, *Sci. Rep.*, 10, 10907
- Ostberg, C., Kane, S. R., Lincowski, A. P., & Dalba, P. A. 2023, *AJ*, 166, 213
- Owen, J. E. 2019, *AREPS*, 47, 67
- Palandri, J. L. & Kharaka, Y. K. 2004, *USGS OFR 2004-1068*
- Pavlov, A. A. & Kasting, J. F. 2002, *Astrobiology*, 2, 27
- Paynter, D. J., Ptashnik, I. V., Shine, K. P., et al. 2009, *JGR Atmospheres*, 114
- Petkowski, J. J., Seager, S., Grinspoon, D. H., et al. 2024, *Astrobiology*, 24, 343
- Petrosyan, A., Galperin, B., Larsen, S. E., et al. 2011, *Rev. Geophys.*, 49, RG3005
- Plotnykov, M. & Valencia, D. 2020, *MNRAS*, 499, 932
- Ptashnik, I. V., McPheat, R. A., Shine, K. P., Smith, K. M., & Williams, R. G. 2011, *JGR Atmospheres*, 116
- Rackham, B. V., Espinoza, N., Berdyugina, S. V., et al. 2023, *RASTI*, 2, 148
- Ramirez, R. M. 2018, *Geosciences*, 8, 280
- Rauer, H., Gebauer, S., Paris, P. V., et al. 2011, *A&A*, 529, A8
- Scheucher, M., Wunderlich, F., Grenfell, J. L., et al. 2020, *ApJ*, 898, 44
- Schlecker, M., Apai, D., Lichtenberg, T., et al. 2024, *PSJ*, 5, 3
- Schubert, G., Turcotte, D. L., & Olson, P. 2001, *Mantle convection in Earth and Planets* (Cambridge, England: Cambridge University Press)
- Schulze, J. G., Wang, J., Johnson, J. A., et al. 2021, *PSJ*, 2, 113
- Schwartzman, D. W. & Volk, T. 1989, *Nature*, 340, 457
- Schwartzman, D. W. & Volk, T. 1991, *GPC*, 4, 357
- Schwieterman, E. W., Kiang, N. Y., Parenteau, M. N., et al. 2018, *Astrobiology*, 18, 663
- Schwieterman, E. W. & Leung, M. 2024, *RiMG*, 90, 465
- Schwieterman, E. W., Reinhard, C. T., Olson, S. L., et al. 2019, *ApJ*, 874, 9
- Sergeev, D. E., Boutle, I. A., Lambert, F. H., et al. 2024, *ApJ*, 970, 7
- Sergeev, D. E., Faucher, T. J., Turbet, M., et al. 2022a, *PSJ*, 3, 212
- Sergeev, D. E., Lewis, N. T., Lambert, F. H., et al. 2022b, *PSJ*, 3, 214
- Shine, K. P., Campargue, A., Mondelain, D., et al. 2016, *JMS*, 327, 193
- Shorttle, O., Jordan, S., Nicholls, H., Lichtenberg, T., & Bower, D. J. 2024, *ApJ*, 962, L8
- Sleep, N. H. & Zahnle, K. 2001, *J. Geophys. Res.*, 106, 1373
- Snellen, I. A. G., de Kok, R. J., le Poole, R., Brogi, M., & Birkby, J. 2013, *ApJ*, 764, 182
- Spake, J. J., Sing, D. K., Evans, T. M., et al. 2018, *Nature*, 557, 68
- Stolzenbach, A., Lefèvre, F., Lebonnois, S., & Määttä, A. 2023, *Icarus*, 395, 115447
- Tian, F. 2015, *AREPS*, 43, 459
- Tosi, N., Godolt, M., Stracke, B., et al. 2017, *A&A*, 605, A71
- Turbet, M., Faucher, T. J., Leconte, J., et al. 2023, *A&A*, 679, A126
- Unterborn, C. T. & Panero, W. R. 2019, *JGR Planets*, 124, 1704
- Way, M. J., Aleinov, I., Amundsen, D. S., et al. 2017, *ApJS*, 231, 12
- Way, M. J. & Del Genio, A. D. 2020, *JGR Planets*, 125, e2019JE006276
- Wilson, C. F., Marq, E., Gillmann, C., et al. 2024, *Space Sci. Rev.*, 220, 31
- Wunderlich, F., Godolt, M., Grenfell, J. L., et al. 2019, *A&A*, 624, A49
- Wunderlich, F., Scheucher, M., Godolt, M., et al. 2020, *ApJ*, 901, 126
- Yates, J. S., Palmer, P. I., Manners, J., et al. 2020, *MNRAS*, 492, 1691

Appendix A: Testing the observability of the end of habitability with a simplified atmosphere model

In this section, we use a simple atmospheric model to characterise a rocky planet evolving out of habitability. Figure A.1 shows the two-step pressure–temperature profiles for the abiotic scenarios 3 and 4 (Table 3), where we followed the approach of Graham & Pierrehumbert (2020) to calculate the pressure–temperature profile. We assumed that the entire surface water reservoir has evaporated and that the planet enters a steam-dominated state with vigorous vertical mixing. For such a state, we further assumed equilibrium between H_2O evaporation and condensation as well as uniform H_2O volume mixing ratios throughout the atmosphere. This results in water volume mixing ratios of 24% in scenario 3 and 97% in moist scenario 4. Consequently, the pressure–temperature profile follows mostly a moist adiabat in the troposphere above the surface. For the very extended atmosphere in moist scenario 4, the pressure–temperature profile starts with a dry adiabat and enters a moist adiabat, dominated by water condensation for pressures ≤ 1 bar (Figure A.1).

Steam-dominated atmospheres are subject to strong atmospheric erosion, where an Earth-like planet around a Sun-like star is expected to lose its total water reservoir within 100 million years (Abe et al. 2011; Hamano et al. 2013). For rocky planets in the habitable zone of the active M dwarf TRAPPIST-1, an Earth-like surface water reservoir is expected to be removed even faster (e.g. Barth et al. 2021; Lincowski et al. 2023). Thus, as an endstate of the planet’s evolution, we assumed the CO_2 dominated desiccated scenario 4, for which all H_2O is removed from steam scenario 4. We further imposed a weak temperature gradient of $7\text{K}/\ln(p)$ in the radiatively dominated upper atmosphere for the desiccated atmosphere, as observed for Venus, for example, with the Magellan space craft and Pioneer Venus (Jenkins et al. 1994). The opacity sources of the absorbers used in this study are listed in Table A.1. For the abiotic cases, we assumed pressure broadening by CO_2 and H_2O , because 1 bar N_2 is a minor constituent for these cases.

Table A.1. Details on opacity sources.

Data type	Data source	Ref.
H_2O broadened by 1 bar N_2 (biotic ^c), H_2O and CO_2^a (abiotic)	HITRAN2020	(1)
CO_2 broadened by 1 bar N_2 (biotic ^c), CO_2 and H_2O (abiotic)	HITRAN2020	(1)
	CAVIAR ^b	(2,3,4)
H_2O continuum	MT_CKD	(5)
	Baranov 2008	(6)
	Odintsova 2020	(7)
CO_2 continuum	MT_CKD	(8)
O_3 broadened by 1 bar N_2	HITRAN2020	(1)
CH_4 broadened by 1 bar N_2	HITRAN2020	(1)

Notes: *a*: We used air broadening coefficients as a proxy for CO_2 broadening since CO_2 broadening of H_2O parameters were not available in HITRAN2020; *b*: Details on the H_2O continuum data used from the CAVIAR laboratory experiment can be found in Anisman et al. (2022); *c*: Biotic cases contain 0.2 bar O_2 ; ⁽¹⁾Gordon et al. (2022), ⁽²⁾Ptashnik et al. (2011), ⁽³⁾Shine et al. (2016), ⁽⁴⁾Paynter et al. (2009), ⁽⁵⁾Mlawer et al. (2012), ⁽⁶⁾Baranov et al. (2008), ⁽⁷⁾Odintsova et al. (2020), ⁽⁸⁾Mlawer et al. (2012)

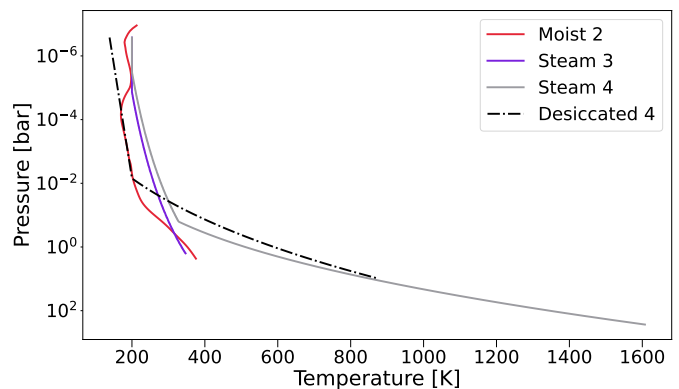


Fig. A.1. Pressure–temperature profiles used to explore the end of habitability. We show steam-dominated scenarios 3 (purple) and 4 (grey) and a desiccated scenario 4 (black dashed-dotted). For comparison, the moist scenario 2 is shown in red.

A comparison between the pressure–temperature profile computed with 1D-TERRA for the moist 2 scenario compared to scenarios 3 and 4 constructed with a two-component toy model shows interesting similarities (Figure A.1). For example, the upper atmosphere profile of the desiccated scenario 4 and the moist 2 scenario for $p \leq 10^{-2}$ bar are very similar despite different atmosphere compositions. Conversely, the latent heat release of more than 10% water vapour in the steam-dominated atmospheres (scenarios 3 and 4) shifts the upper atmosphere profiles to higher temperatures compared to the moist scenario 2 with $\text{VMR}_{\text{H}_2\text{O}} \approx 10^{-4}$ in the upper atmosphere (Figure 4, bottom). This comparison highlights the challenge to distinguish between different atmosphere scenarios of rocky planets in the presence of a high altitude cloud top ($p \leq 10^{-2}$ bar).

Appendix B: Observability of the uninhabitable end-states

In the following, we explore the observational signature of H_2O - CO_2 dominated and desiccated CO_2 atmosphere scenarios with petiTDRTRANS for various JWST observation modes, starting with the cloud-free case. For clarity, we simulated the expected noise from JWST observations with PANDEXO for only one scenario applied to TRAPPIST-1e. We chose the steam 3 scenario for 100 transmission and the dry biotic scenarios for 10 eclipse observations, respectively.

Figure B.1 (top) shows that the transition from the moist towards the thick steam-dominated atmosphere regime is mostly heralded by an increase in pressure broadening of the CO_2 absorption feature at $4.3 \mu\text{m}$. For the desiccated CO_2 scenario 4, it is also apparent that this extreme broadening is accompanied by a flattening of the overall transmission spectrum between $3\text{--}5 \mu\text{m}$ – even when neglecting the impact of clouds. In the MIRI wavelength range, the water opacities become dominant for the steam atmosphere scenarios between $5\text{--}8 \mu\text{m}$ (Figure B.1, centre). However, even for the cloud-free steam-dominated scenario 4, the H_2O amplitude is above 3σ for an accuracy of 20 ppm with 100 JWST transits. The prominent CO_2 spectral features in the desiccated scenario 4 are below 2σ .

In the cloud-free case, emission spectra appear to be more promising to differentiate between habitable and uninhabitable climate states. Figure B.1 (bottom) demonstrates that O_3 signatures between 9 and $10 \mu\text{m}$ could be detectable to an accuracy of 3σ already with 10 JWST eclipse observations. The biosignature of CH_4 at $7.7 \mu\text{m}$ is at about 2.5σ significance for 10

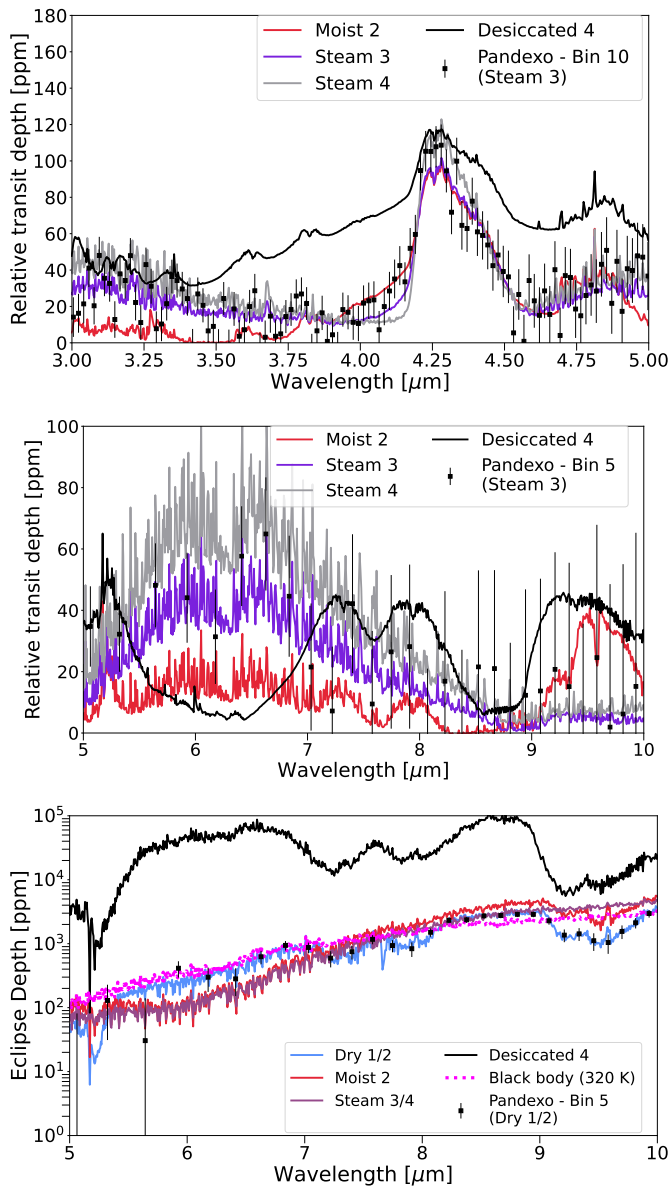


Fig. B.1. Transmission and eclipse data. The top and centre panels show transmission spectra for moist scenario 2 (red), steam scenarios 3 (purple) and 4 (grey), and the desiccated scenario 4 (black) for the JWST/NIRSpec wavelength range 3 – 5 μm (top) and the JWST/MIRI wavelength range between 5 – 10 μm (centre) with simulated noise (black error bars). We chose the G395M grism setting with 10 pixels per bin (top) and the MIRI LRS setting with 5 pixels per bin (centre). The bottom panel shows eclipse spectra for cloud-free atmospheres for the dry biotic scenarios 1/2 (blue), the moist biotic scenario 2 (red), the abiotic steam scenarios 3/4 (purple), and the desiccated scenario 4 (black) for the JWST/MIRI wavelength range 5 – 10 μm with simulated noise (black error bars), where we combined 5 pixels per bin.

observations. Thus, in principle, the signatures of biotic atmospheres could be achievable with relative little time investment with eclipse observations to justify further observations to identify CH_4 and H_2O . An uninhabitable desiccated CO_2 atmosphere should be easily discernible as well. This conclusion only holds if the atmosphere is cloud-free or at least does not exhibit a thick, continuous cloud coverage, however.

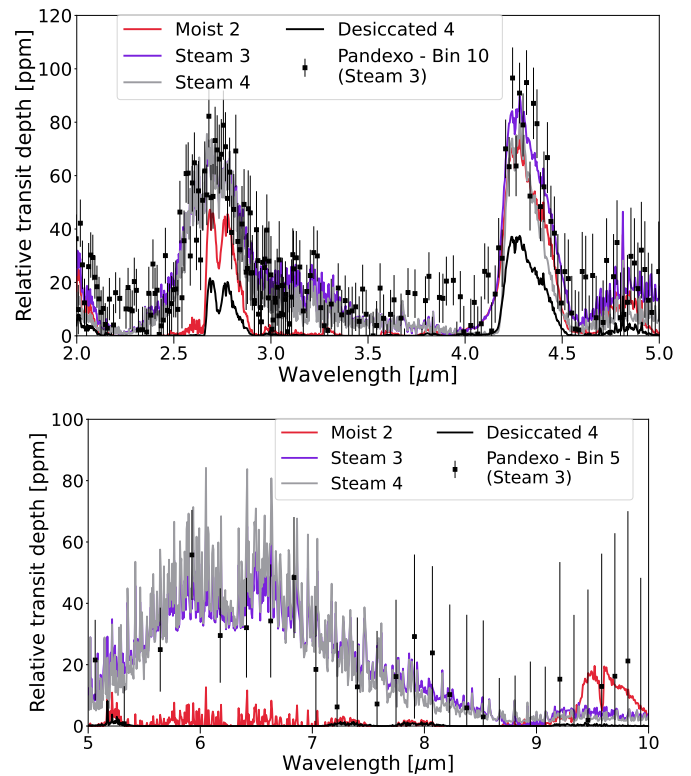


Fig. C.1. Cloudy transmission spectra. We illustrate the moist, biotic scenario 2 (red), the abiotic steam scenarios 3 (purple) and 4 (grey), and the desiccated scenario 4 for the JWST/NIRSpec wavelength range 3 – 5 μm (top) and the JWST/MIRI wavelength range between 5 – 10 μm (bottom) with simulated noise (black error bars). We chose the G235M (2-3 μm) and G395M grism setting (3-5 μm), each with 10 pixels per bin (top), and the MIRI LRS setting with 5 pixels per bin (bottom).

Appendix C: Impact of clouds on the observability of the uninhabitable end states

While the results of the previous section suggest that at least to first order insights about the atmospheric composition could be obtained using JWST transmission and emission spectra, the impact of clouds and of 3D circulation have been neglected, which can affect O_3 concentrations (Carone et al. 2018; Chen et al. 2019, 2021). For simplicity, we here adopted a continuous, grey cloud deck scenario at $p = 0.01$ bar, which represents a thick cumulonimbus cloud for Earth-like atmospheres and the top of the sulphur clouds on Venus (e.g. Cimino 1982). We again simulated the expected noise from JWST observations with PANDEXO for only one scenario applied to TRAPPIST-1e and chose the steam 3 scenario for 100 transmission and the dry biotic scenarios for 10 eclipse observations, respectively.

From the NIRSpec transmission spectrum (Figure C.1 top), it is evident that a sufficiently high cloud deck reduces all atmospheric features, including the CO_2 feature. Interestingly, a very extended CO_2 dominated atmosphere has the smallest atmospheric features of all explored scenarios. Furthermore, the abiotic steam scenario 4 and the moist biotic scenario 2 would only be distinguishable by the larger water content of the first between 2.5 and 3 micron. Here, however, one would have to ensure that the water feature indeed stems from the atmosphere and not from the host star (Lim et al. 2023). The transmission spectra in the MIRI wavelength range between 5-10 micron would be more illuminating (Figure C.1 top). Here, the steam scenarios

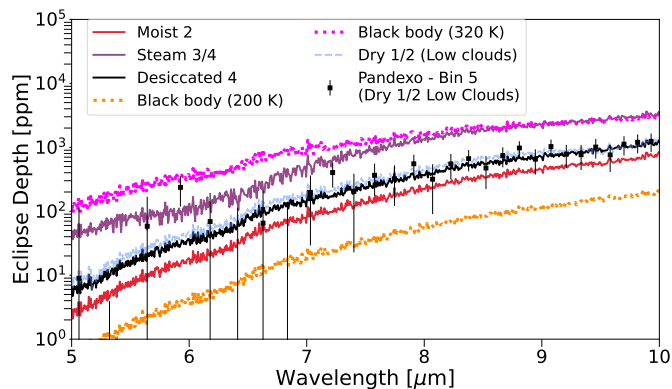


Fig. C.2. Cloudy eclipse spectra. We show the dry biotic scenarios 1/2 (blue), the moist biotic scenario 2 (red), the abiotic steam scenarios 3/4 (purple), the dry biotic scenario with low clouds (dashed blue), and the desiccated scenario 4 (black) for the JWST/MIRI wavelength range 5–10 μm combining 5 pixels per bin (black error bars).

would in principle be differentiable by the H_2O feature between 5–10 micron. The biotic moist scenario 2 would be identifiable by the O_3 feature at 9.8 μm . However, the strength of that signal is less than 20 ppm and thus less than 1σ even with 100 transit observations. Only the thick steam atmosphere of the abiotic scenario 4 exhibits a water signature of about 3σ . Interestingly, the transmission spectrum between 5 and 10 μm for a CO_2 -dominated atmosphere of the desiccated scenario 4 is rendered flat by clouds with atmospheric features even below 10 ppm.

The impact of clouds is even more pronounced for measurements focusing on resolving the thermal flux of the planet during the secondary eclipse (Figure C.2). For these measurements, we tested for the dry scenarios 1 and 2 a low cloud top at 0.1 bar. We further simulated JWST observations with PANDEXO for the biotic scenario with low clouds with MIRI LRS, assuming 10 eclipse observations of TRAPPIST-1e. The only remaining noticeable atmospheric feature after a cloud deck was applied is the broad H_2O feature, which is about 2σ for 10 JWST observations. When the cloud deck was placed high enough ($\leq 10^2$ bar), the differences in the upper atmosphere temperatures become important. We spanned a relatively large range between cool upper atmospheres with 200–250 K for the desiccated CO_2 -dominated and the biotic, habitable atmosphere scenarios (1&2) and the 320 K warm upper atmosphere for the steam-dominated or runaway-greenhouse atmospheres (scenarios 3 and 4).

For the eclipse measurements, two properties of the upper atmosphere are important. Lower temperatures result in a smaller overall thermal flux from the planet, scaling with T^4 . At the same time, the low temperature gradient in the upper atmosphere suppresses molecular features like the biosignatures CH_4 and O_3 . Atmospheric characterisation with eclipse measurements will thus only be feasible for runaway greenhouse atmospheres, steam atmospheres, or for atmospheres that are either occasionally cloud-free or exhibit a noncontinuous cloud coverage that allows to resolve the planetary thermal flux from deeper parts of the planetary atmosphere. Otherwise, in the presence of a thick cloud deck, the desiccated scenario 4 with its CO_2 -dominated atmosphere is indistinguishable from biotic habitable scenarios 1 and 2.

Last but not least, we note that the steam scenario 4 has surface temperatures that exceed 1200 K (Figure A.1), which is the melting point of silicate rock (Kasting 1988). In such a case, a release of SO_2 from the surface into the atmosphere could be expected (Janssen et al. 2023).

Appendix D: 1D-TERRA

A detailed 1D atmosphere chemistry model sheds more light on the atmosphere composition and observability of the different scenarios. We used the 1D climate-chemistry model 1D-TERRA which is a global mean, stationary, cloud-free, radiative-convective photochemical model extending from the planetary boundary layer, specifically, from a height of 0.5 km above the surface to the lower thermosphere (Pavlov & Kasting 2002; Rauer et al. 2011; Gebauer et al. 2018). As outlined in Wunderlich et al. (2020), the code has the capability to explore wet and dry climates, motivated by different near-surface assumptions about rain-out in the atmospheric planetary boundary layer (see also Appendix E). As a result, the near-surface temperatures may vary due to the strong greenhouse effect of water vapour.

The flexible radiative transfer module REDFOX is described and validated for modern Earth, Venus, and Mars in Scheucher et al. (2020). REDFOX applies the correlated-k distribution method with 128 spectral bands from 100.000 to zero wavenumbers including 20 main absorbers from HITRAN2016 (Gordon et al. 2017) and 81 absorbers in the FUV to visible from the Max Planck Institute (MPI) Spectral Atlas. Collision-induced absorption coefficients were taken from HITRAN2016 and Rayleigh scattering was included for 8 species. Relative humidity profiles were taken from Manabe & Wetherald (1967).

The photochemistry module BLACKWOLF was developed for atmospheres dominated by N_2 , CO_2 , H_2 , and H_2O . The scheme features 1127 chemical reactions for 128 species. Photochemical reactions for 81 absorbers are considered in 133 bands from 100–850 nm. Rate data were taken from the JPL Report 18 (Burkholder et al. 2015) and the National Institute of Standards and Technology (NIST) Version 6 (Mallard et al. 1994). BLACKWOLF has been validated for modern Earth, Venus and Mars in Wunderlich et al. (2020). Eddy mixing can be calculated flexibly as described in Wunderlich et al. (2020).

A straightforward thermal escape rate for H and O is prescribed in the upper model lid. The lower boundary condition for each chemical species can be set up as a fixed mixing ratio or by source and loss fluxes.

Appendix E: Atmospheric planetary boundary layer

In this work, we connected the outputs of an evolution model of rocky planets, focussing on long-term processes in the mantle, with the surface as the upper boundary and including a simplified atmosphere response, to a detailed 1D atmosphere model (1D TERRA). Coupling these two models, in particular for a case that evolves out of the present-day Earth-like regime, is challenging as it includes the ‘planetary boundary layer (PBL) problem’. The PBL, extending around 1 km on Earth and 10 km on Mars (Petrosyan et al. 2011), requires detailed treatment of microphysical surface processes such as energy transfer via conduction and convection, turbulence, and water condensation and evaporation, which determines the efficiency of the water cycle and the near-surface latent heat flux. While for present-day Earth, these properties are well measured, they are far less constrained for other planets. For a study on surface friction within the PBL for tidally-locked Exo-Earths, the reader is referred to Carone et al. (2016).

Improving the connection between the geophysical and atmospheric models is desirable, yet near-surface conditions are accessible only through in situ measurements, which are currently limited to Solar System planets. Additionally, the conditions of near surface ocean condensation on tidally locked ex-

oplanets (Turbet et al. 2023) like TRAPPIST-1e and of moist convection, water vapour transport throughout the free 3D atmosphere, are currently debated (Sergeev et al. 2024). For example, four different 3D climate models for TRAPPIST-1e produce different results in cloud coverage and precipitation under identical irradiation and composition settings (Sergeev et al. 2022a). Godolt et al. (2016) point out that for Earth-like atmospheres with increased irradiation, as explored here, the 1D atmosphere model TERRA underestimates the relative humidity compared to 3D climate models when using the Earth-like humidity profiles of Manabe & Wetherald (1967). To address these uncertainties, we here adopted two extreme water cycle scenarios in 1D TERRA.

We assumed that the geophysical model captures the surface conditions, including a water vapour-rich near-surface atmospheric layer at the base of the PBL. 1D TERRA then links the surface conditions, mainly above the PBL, to the observable atmosphere, with parameterisations within the PBL to capture parts of the water cycle. The model begins with 1 point at 0.5 km altitude within the PBL. For the dry regimes, we used profiles of Manabe & Wetherald (1967), assuming most water rains out below the model domain (first 0.5 km), leaving a VMR of water of 10^{-6} in the gas phase. The water removed from the gas phase no longer contributes to the greenhouse effect above the rain-out region, resulting in a different temperature at the lower boundary of the pressure-temperature profile at 0.5 km compared to the geophysical model at 0 km height. For the moist regime, only 10% of the water was assumed to rain-out below the modelling domain, leaving a VMR of water of about 10^{-1} in the gas phase above the rain-out region. These two extreme scenarios highlight the importance of the water cycle in the detectability of methane as a potential biosignature.